

NAVAL POSTGRADUATE SCHOOL

Monterey, California



THESIS

366857

THERMOMECHANICAL PROCESSING OF A1 ALLOY 2090
FOR GRAIN REFINEMENT AND SUPERPLASTICITY

by

Procopios T. Spiropoulos

December 1987

Thesis Advisor:

T. R. McNelley

Approved for public release; distribution is unlimited.

T239249

REPORT DOCUMENTATION PAGE

1a REPORT SECURITY CLASSIFICATION UNCLASSIFIED		1b RESTRICTIVE MARKINGS	
2a SECURITY CLASSIFICATION AUTHORITY		3 DISTRIBUTION/AVAILABILITY OF REPORT Approved for public release; distribution is unlimited.	
2b DECLASSIFICATION/DOWNGRADING SCHEDULE		4 MONITORING ORGANIZATION REPORT NUMBER(S)	
4 PERFORMING ORGANIZATION REPORT NUMBER(S)		5 MONITORING ORGANIZATION REPORT NUMBER(S)	
6a NAME OF PERFORMING ORGANIZATION Naval Postgraduate School	6b OFFICE SYMBOL (If applicable) 33	7a NAME OF MONITORING ORGANIZATION Naval Postgraduate School	
6c ADDRESS (City, State, and ZIP Code) Monterey, California 93943-5000		7b ADDRESS (City, State, and ZIP Code) Monterey, California 93943-5000	
8a NAME OF FUNDING SPONSORING ORGANIZATION	8b OFFICE SYMBOL (If applicable)	9 PROCUREMENT INSTRUMENT IDENTIFICATION NUMBER	
8c ADDRESS (City, State, and ZIP Code)		10 SOURCE OF FUNDING NUMBERS	
		PROGRAM ELEMENT NO	PROJECT NO
		TASK NO	WORK UNIT ACCESSION NO
11 TITLE (Include Security Classification) THERMOMECHANICAL PROCESSING OF Al ALLOY 2090 FOR GRAIN REFINEMENT AND SUPERPLASTICITY			
12. PERSONAL AUTHOR(S) Spiropoulos, Procopios T.			
13a TYPE OF REPORT Master's Thesis	13b TIME COVERED FROM _____ TO _____	14 DATE OF REPORT (Year, Month, Day) 1987, December	15 PAGE COUNT
16. SUPPLEMENTARY NOTATION			
17 COSATI CODES		18 SUBJECT TERMS (Continue on reverse if necessary and identify by block number)	
FIELD	GROUP	SUB-GROUP	
19 ABSTRACT (Continue on reverse if necessary and identify by block number) An Al-Cu-Li-Zr alloy, recently registered as 2090, with 7 percent lower density and 10 percent higher elastic modulus, has been introduced as a replacement for the 7075-T6 alloy. The purpose of this research is to investigate the applicability of thermomechanical processing methods developed at NPS for materials including Al-Mg and Al-Mg-Li alloys, to the 2090 alloy. The material is hot worked, cold worked, aged and warm rolled to a total true strain of about 2.4. Tensile tests were conducted at different temperatures and strain rates allowing a determination of the effect of the processing on microstructural evolution and the super-plastic behavior of this material.			
20 DISTRIBUTION/AVAILABILITY OF ABSTRACT <input checked="" type="checkbox"/> UNCLASSIFIED/UNLIMITED <input type="checkbox"/> SAME AS RPT <input type="checkbox"/> DTIC USERS		21 ABSTRACT SECURITY CLASSIFICATION UNCLASSIFIED	
22a NAME OF RESPONSIBLE INDIVIDUAL T. R. McNelley		22b TELEPHONE (Include Area Code) (408) 646-2589	22c OFFICE SYMBOL 69Mc

Approved for public release; distribution unlimited

Thermomechanical Processing of Al Alloy 2090
for Grain Refinement and Superplasticity

by

Procopios T. Spiropoulos
Captain, Hellenic Air Force
B.S., Hellenic Air Force Academy, 1977
B. S., Electrical Engineering, Univ of Patras, 1981

Submitted in partial fulfillment of the
requirements for the degree of

MASTER OF SCIENCE IN MECHANICAL ENGINEERING

from the

NAVAL POSTGRADUATE SCHOOL
December 1987

ABSTRACT

An Al-Cu-Li-Zr alloy, recently registered as 2090, with 7 percent lower density and 10 percent higher elastic modulus, has been introduced as a replacement for the 7075-T6 alloy. The purpose of this research is to investigate the applicability of thermomechanical processing methods developed at NPS for materials including Al-Mg and Al-Mg-Li alloys, to the 2090 alloy. The material is hot worked, cold worked, aged and warm rolled to a total true strain of about 2.4. Tensile tests were conducted at different temperatures and strain rates allowing a determination of the effect of the processing on microstructural evolution and the superplastic behavior of this material.

TABLE OF CONTENTS

Thesis
504857
C-1

I.	INTRODUCTION	11
II.	BACKGROUND	13
A.	ALUMINUM ALLOY SYSTEMS	13
1.	Aluminum-Copper System	13
2.	Aluminum-Lithium System	14
3.	Aluminum-Zirconium System	16
4.	Aluminum-Copper-Lithium-Zirconium System	18
B.	ALITHALITE ALLOY 2090	21
C.	SUPERPLASTICITY	22
D.	PREVIOUS INVESTIGATIONS AT NPS	28
E.	OBJECTIVE OF THIS RESEARCH	29
III.	EXPERIMENTAL PROCEDURE	31
A.	MATERIAL	31
B.	THERMOMECHANICAL PROCESSING	31
1.	Solution Treatment and Upset Forging	32
2.	Cold Working	34
3.	Aging	34
4.	Warm Working	34
C.	MECHANICAL TESTING	36
D.	METALLOGRAPHY	39
IV.	RESULTS AND DISCUSSION	40
A.	EFFECT OF PROCESSING ON MICROSTRUCTURE	40
1.	Optical Microscopy Results	40

a. Aging Time Effect	40
b. Reheating Time Effect	41
2. Transmission Electron Microscopy Results	48
a. As-Rolled Microstructure	48
b. Effect of Heating at 300 C	53
B. MECHANICAL PROPERTIES	59
1. Stress vs Strain Response	59
2. Ductility, Stress vs Strain Rate Response	59
3. Stress, Ductility vs Temperature Response	64
C. MICROSTRUCTURAL ANALYSIS OF DEFORMED CONDITIONS	64
D. PHASES OBSERVED	71
V. CONCLUSIONS	73
VI. RECOMMENDATIONS	75
APPENDIX A. COMPUTER PROGRAM	76
APPENDIX B. TENSILE TEST DATA	77
REFERENCES	82
INITIAL DISTRIBUTION LIST	85

LIST OF TABLES

1. Composition of 2090 , wt%	23
2. Physical properties of 2090	23
3. Mechanical Properties of 2090	23
4. Sample Composition , wt%	31
5. Thermomechanical Processing Schedule	32
6. Conditions used for Tensile Testing	38
7. Possible Phases in 2090	72

LIST OF FIGURES

2.1	Aluminum-Copper Phase Diagram	15
2.2	Aluminum-Lithium Phase Diagram	17
2.3	Aluminum-Zirconium Phase Diagram	19
2.4	Aluminum corner of the Aluminum-Copper-Lithium Phase Diagram; phase distribution at 502°C (solid lines) and 327°C (dashed lines)	20
2.5	Stress versus Strain Rate. Shape of curves that different materials exhibit during Superplastic deformation	25
3.1	Thermomechanical Processing Techniques	33
3.2	Partial Aluminum-Lithium Phase Diagram with TMP regions indicated	35
4.1	Optical micrographs, (a) bright field, (b) dark field, of alloy 2090 in the as-rolled condition processed by TMP 1.	42
4.2	Optical micrographs, (a) bright field, (b) dark field, of alloy 2090 in the as-rolled condition processed by TMP 4.	43
4.3	Optical micrographs, (a) bright field, (b) dark field, of alloy 2090 in the as-rolled condition processed by TMP 2.	44
4.4	Optical micrographs, (a) bright field, (b) dark field, of alloy 2090 in the as-rolled condition processed by TMP 6.	45
4.5	Optical micrographs, (a) bright field, (b) dark field, of alloy 2090 in the as-rolled condition processed by TMP 3.	46
4.6	Optical micrographs, (a) bright field, (b) dark field, of alloy 2090 in the as-rolled condition processed by TMP 7.	47
4.7	Bright field TEM micrographs, of alloy 2090 in the as-rolled condition processed by TMP 2.	49
4.8	Bright field TEM micrograph, of alloy 2090 in the as-rolled condition processed by TMP 2.	50

4.9	Bright field TEM micrographs, of alloy 2090 in the as-rolled condition processed by TMP 6.	51
4.10	Bright field TEM micrograph, of alloy 2090 in the as-rolled condition processed by TMP 6.	52
4.11	Bright field TEM micrographs, of alloy 2090 from the grip section of a tensile sample tested at 300°C and $1.67 \times 10^{-1} \text{ S}^{-1}$ strain rate processed by TMP 2.	54
4.12	Bright field TEM micrograph, of alloy 2090 from the grip section of a tensile sample tested at 300°C and $1.67 \times 10^{-1} \text{ S}^{-1}$ strain rate processed by TMP 2.	55
4.13	Bright field TEM micrograph, of alloy 2090 from the grip section of a tensile sample tested at 300°C and $1.67 \times 10^{-1} \text{ S}^{-1}$ strain rate processed by TMP 6.	57
4.14	Bright field TEM micrographs, of alloy 2090 from the grip section of a tensile sample tested at 300°C and $6.67 \times 10^{-4} \text{ S}^{-1}$ strain rate processed by TMP 6.	58
4.15	True stress versus true strain for tensile testing conducted at 300°C, for material processed by TMP 2, at various strain rates.	60
4.16	True stress versus true strain for tensile testing conducted at 300°C, for material processed by TMP 6, at various strain rates.	61
4.17	Ductility versus strain rate for tensile testing conducted at 300°C, for material processed by TMP 1, TMP 2, TMP 6, TMP 7.	62
4.18	True stress at 0.1 strain versus strain rate for tensile testing conducted at 300°C for material processed by TMP 1, TMP 2, TMP 6, TMP 7.	63
4.19	True stress at 0.1 strain and $6.67 \times 10^{-4} \text{ S}^{-1}$ strain rate versus temperature. Comparison between TMP 2 and TMP 6.	65
4.20	Ductility at $6.67 \times 10^{-4} \text{ S}^{-1}$ strain rate versus temperature. Comparison between TMP 2 and TMP 6.	66
4.21	Bright field TEM micrographs, of alloy 2090 from the gage section of a tensile sample tested at 300°C and $6.67 \times 10^{-4} \text{ S}^{-1}$ strain rate.	67

4.22	TEM micrographs, (a) bright field, (b) dark field, of alloy 2090 from the gage section of a tensile sample tested at 300°C and $6.67 \times 10^{-4} \text{ S}^{-1}$ strain rate processed by TMP 2.	68
4.23	Bright field TEM micrographs, of alloy 2090 from the gage section of a tensile sample tested at 300°C and $6.67 \times 10^{-4} \text{ S}^{-1}$ strain rate processed by TMP 6.	69
4.24	TEM micrographs, (a) bright field, (b) dark field, of alloy 2090 from the gage section of a tensile sample tested at 300°C and $6.67 \times 10^{-4} \text{ S}^{-1}$ strain rate processed by TMP 6.	70
B.1	True stress versus true strain for tensile testing conducted at 300°C, for material processed by TMP 1 at various strain rates.	77
B.2	True stress versus true strain for tensile testing, conducted at 300°C, for material processed by TMP 7.	78
B.3	True stress at $6.67 \times 10^{-4} \text{ S}^{-1}$ strain rate versus true strain for tensile testing conducted at 370°C, for material processed by TMP 2 and TMP 6.	79
B.4	True stress at $6.67 \times 10^{-4} \text{ S}^{-1}$ strain rate versus true strain for tensile testing conducted at 440°C, for material processed by TMP 2 and TMP 6.	80
B.5	True stress at $6.67 \times 10^{-4} \text{ S}^{-1}$ strain rate versus true strain for tensile testing conducted at 510°C, for material processed by TMP 2 and TMP 6.	81

ACKNOWLEDGMENT

I would like to thank my advisor, Professor T. R. McNelley, and Dr. S. J. Hales for the expert, tireless assistance and guidance they provided during my research. Also, I want to thank my friends and co-workers, A. Salama, I. Munro and B. Ferris, for their insight which added depth to my thesis. I would also like to acknowledge the Hellenic Air Force for the opportunity given to me to attend the Naval Postgraduate School and obtain a Master's degree. Finally, I would like to express my sincere appreciation to my wife, Sotiria, and our two children, Panagiota and Nicolaos, for their dedicated support of my work at NPS.

I. INTRODUCTION

Spurred by the competition from other materials such as composites, the Aluminum industry has intensified research in order to retain the airframe structural materials market. Considerable emphasis has been placed on Lithium containing Aluminum alloys owing to weight savings and improved strength capabilities. Lithium decreases the density of Aluminum alloys by three percent for every one weight percent of Lithium added. Used to replace conventional materials, these alloys promise to trim as much as seven tons from an 80 ton jet airliner. The Al-Li alloys look so promising that ALCOA recently expanded its facilities to produce one such alloy called Alithalite for supply to airframe manufacturers. This alloy, 2090, a replacement for 7075 Aluminum, is 7 to 8 percent less dense. Testing also demonstrates 10 percent more stiffness for a given weight and also good superplastic forming capabilities. It is suggested that Aluminum-Lithium based alloys could initially replace alloys 2024, 7075 and 2014, and second generation versions could replace 2124, 7475 and 7050.

Commercial Aluminum-Lithium alloys such as 2090 need to be stretched prior to aging in order to obtain optimum strength and fracture toughness combination. The stretch requirement has been an obstacle to their use as superplastic forming materials. The effect of stretching on the precipitation kinetics and the relationship between precipitate size and distribution and mechanical properties has been a subject of extensive research.

It is possible to induce superplastic behavior in Aluminum-Lithium based alloys, either by the use of the "Rockwell" processing route to yield a fully recrystallized fine grained, structure before commencing superplastic deformation or by employing the "Supral" processing route in which the starting sheet is in a rolled condition before superplastic deformation commences and the fine grain size is generated simultaneously with the forming operation. The goal of this work is to apply the knowledge gained from research on Al-Mg-Li-Zr alloys to the Al-Cu-Li-Zr (2090) alloy using thermomechanical processing which is more closely akin to the "Supral" processing route. The intention is to produce a uniform distribution of fine second phase particles by a combination of cold rolling and aging heat treatments such that a fine-grained structure may be developed from the as-rolled structure. The research on the Al-Mg-Li-Zr alloys has demonstrated superplasticity to be attainable at lower temperatures and higher strain rates than with the "Rockwell" or "Supral" processes. This is the result of a much finer 2-5 μm grain size. Superplastic deformation at lower temperatures with such refined structures appears less susceptible to cavitation, and the refined structures may also alter precipitation kinetics in subsequent precipitation hardening.

II. BACKGROUND

A. ALUMINUM ALLOY SYSTEMS

There are several applications where super-purity aluminum (99.99% Al, minimum) is used, e.g. the manufacturing of electrolytic capacitor foil, but usually when we use the word "Aluminum" we mean an Aluminum alloy. The preeminent reason for alloying Aluminum is to increase the mechanical properties: strength, hardness and resistance to fatigue wear or creep. The major alloying elements used with aluminum are Cu, Mn, Mg, Zn, and now Li.

Unalloyed Aluminum is a single-phase material and in optical microscopic examination only grains and grain boundaries can be seen. Solid solutions formed with pure aluminum, by any of the alloying elements, exhibit the same microstructural appearance. Their phase diagrams with Al have a solid-solution region located at the Aluminum end. When the alloying element content exceeds the solid solubility limit, a second phase is produced the composition of which depends on ratios and total amounts of alloying element present. These phases are more complex in ternary or higher order alloys. Using specific thermomechanical processes the amount, shape, size and distribution of the second phase can be controlled and the alloy can attain specific desirable properties.

1. Aluminum-Copper System

Copper is a basic alloying element for aluminum and forms important families with other alloys. The addition of copper increases

the strength at low temperatures by heat treatment, while at high temperatures by the formation of intermetallic compounds. Binary Al-Cu alloys containing 3% Cu or more exhibit natural aging after solution heat treating and quenching. Strength and hardness increase by increasing both time of natural aging and increasing copper content of the alloy from 3% to the limit of solid solubility (5.65%). During aging of Aluminum-Copper alloys, a series of second phase precipitates form before the stable θ phase is produced. Localized concentrations of copper atoms form GP-I, Guinier-Preston zones, at room temperature enhancing the alloys hardening. GP-I zones consist of two dimensional copper-rich regions of disc-like shape, three to five nm in diameter, oriented on (100) planes. At temperatures of 100°C and higher more copper atoms diffuse until GP-I zones disappear to be replaced by disc-like GP-II zones, or θ'' phase. θ'' phase is three dimensional and has an ordered atomic arrangement. Later θ'' is dissolved and transition plate-like θ' phase forms, semicoherent with the solid solution lattice, having the same composition with the final incoherent, plate-like, stable θ phase (CuAl_2). The precipitation sequence can be written as:

Supersaturated Solid Solution GP-I \rightarrow GP-II or $\theta'' \rightarrow \theta' \rightarrow \theta$.

In Figure 2.1, the binary Aluminum-Copper Phase Diagram is shown. [Ref. 1]

2. Aluminum-Lithium System

Reduced density and increased elastic modulus are the two benefits characteristic of Aluminum-Lithium based alloys which have been quickly and widely recognized. Extensive evaluation of the material has

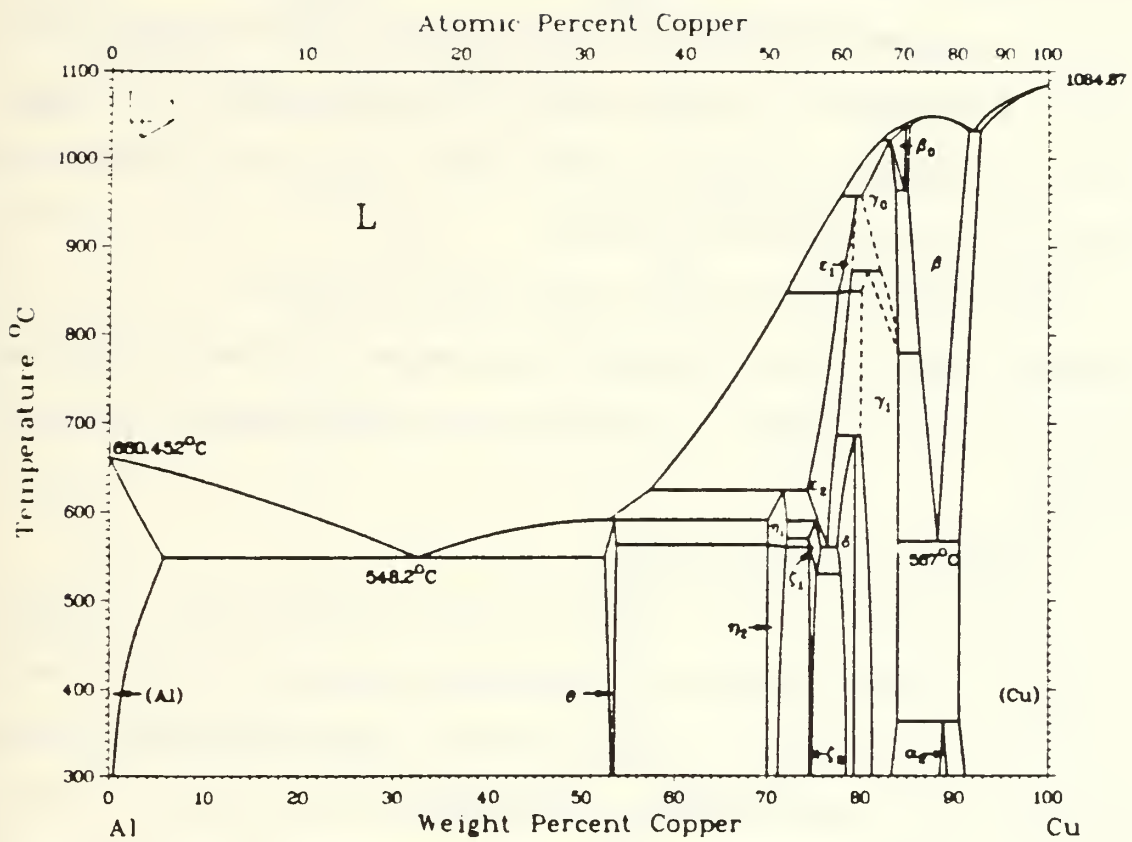
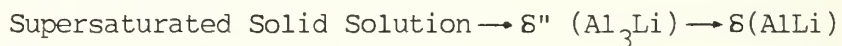


Figure 2.1. Aluminum-Copper Phase Diagram

been carried out by many aircraft manufactures. The addition of up to 4% Li to Al and its alloys improves the strength-to-weight and stiffness-to-weight ratios with each wt % Li, resulting in about 3% reduction in density and 6% increase in Young's modulus [Ref. 2,3]. Aluminum-Lithium alloys rely upon precipitation hardening to develop high-strength and the extensive homogeneous precipitation of the metastable, spheroidal δ' phase (Al_3Li) is widely reported to act as the primary strengthening mechanism [Ref. 3,4]. Dissolution of δ' phase leads to the stable plate-like δ phase (AlLi) and the precipitation sequence can be summarized as follows:



The phase diagram for the Aluminum-Lithium system, proposed by Sigli and Sanchez [Ref. 5] Figure 2.2, shows the two phase boundaries for Al_3Li and AlLi .

3. Aluminum-Zirconium System

Zirconium is a minor addition to some aluminum alloys in which it forms a fine precipitate of intermetallic particles, in the form of Al_3Zr , that control grain size and inhibit recrystallization during fabrication and heat treatment. Zirconium, in the range 0.1 to 0.3%, acts as a grain-refiner and also increases the recrystallization temperature in wrought products of several Aluminum alloy systems. The grain size control through of use zirconium has many purposes, which include high fracture toughness, good forming characteristics, resistance to stress corrosion cracking and superplastic deformation. Al_3Zr precipitates are spheroidal and coherent with lattice. They are

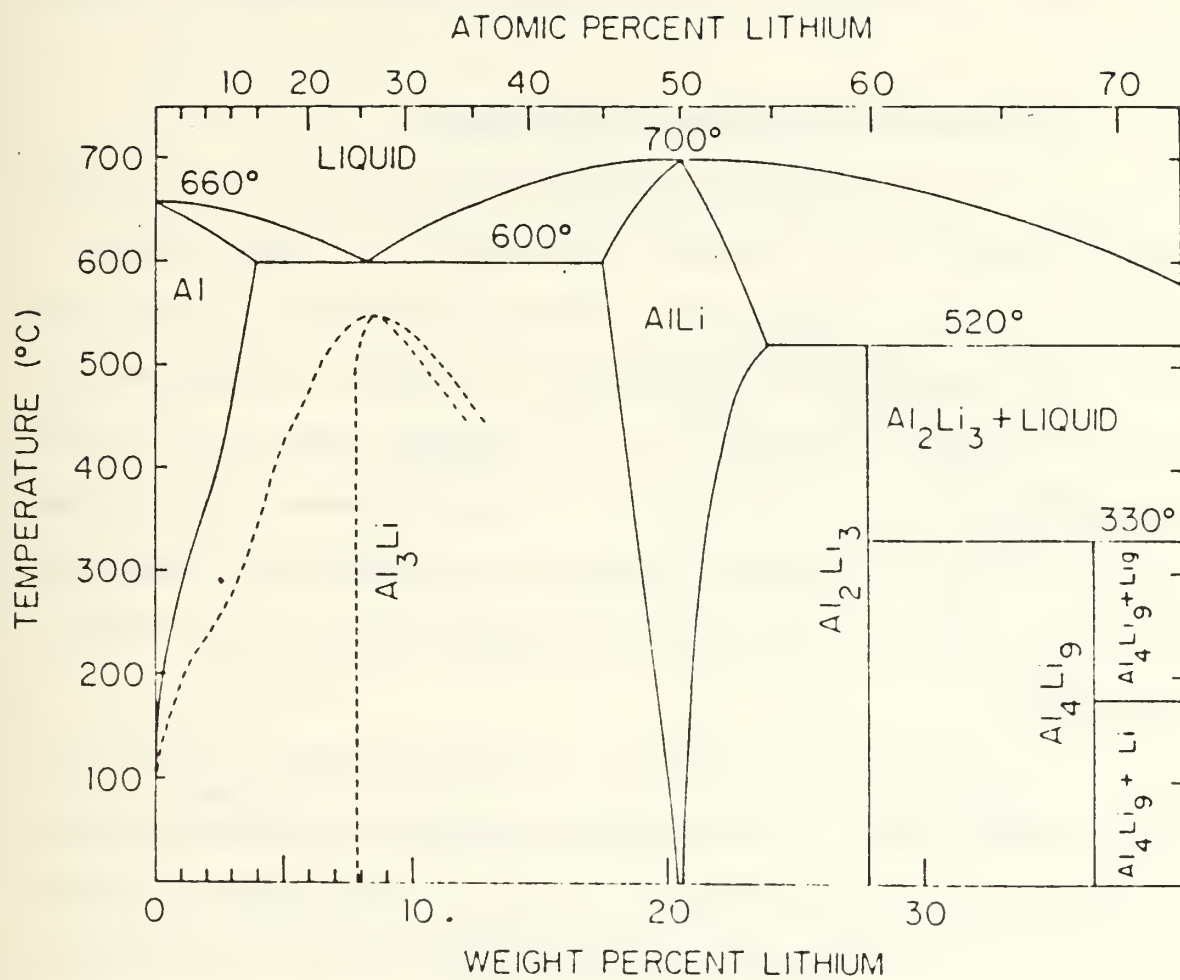


Figure 2.2. Aluminum-Lithium Phase Diagram

small in size, approximately 200 \AA in diameter, [Ref. 6]. These small particles are effective in pinning grain boundaries and slowing down grain growth [Ref. 7,8], even with a quite low volume fraction present in the alloy. In Figure 2.3 the binary Al-Zr phase diagram is shown [Ref. 1].

4. Aluminum-Copper-Lithium-Zirconium System

As in the binary Al-Cu system, the addition of several weight percent Cu to Al-Li alloys increases the strength of these materials, largely through an influence on the stable and metastable equilibria and the related sequence of precipitation reactions. Thermomechanical treatments of these alloys, as is all Aluminum alloys, are usually designed to avoid precipitation of large, incoherent second-phase particles. These are generally thought to be harmful to the mechanical properties of the alloy if they do not have the required shape, size and distribution.

In the aluminum-rich corner of the Aluminum-Copper-Lithium alloy phase diagram, there are three possible compounds in equilibrium namely T_1 , T_2 and T_B , as shown in Figure 2.4 [Ref. 4]. The T_1 phase (Al_2CuLi) has a plate-like morphology shape with a hexagonal crystal structure ($a = 4.97 \text{ \AA}$ and $c = 9.34 \text{ \AA}$). The T_2 phase ($\text{Al}_2\text{Li}_3\text{Cu}$) has a cubic structure ($a = 13.914 \text{ \AA}$) and the T_B phase ($\text{Al}_{7.5}\text{LiCu}_4$) has a cubic structure ($a = 5.83 \text{ \AA}$) [Ref. 10]. A new phase, designation I, of unknown composition has also been reported by Cassada [Ref. 9]. The I-phase exhibits five-fold diffraction symmetry and the mechanism for its formation is nucleation and growth. Several metastable phases have been suggested to

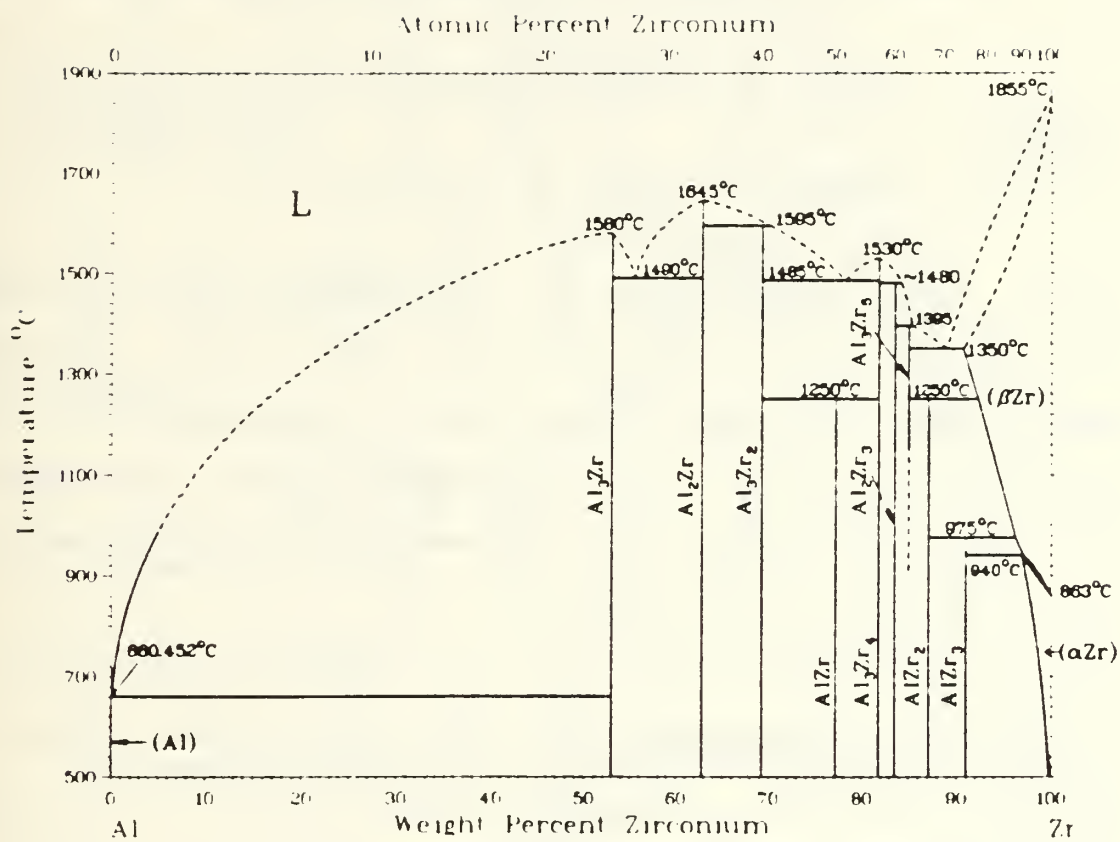


Figure 2.3. Aluminum-Zirconium Phase Diagram

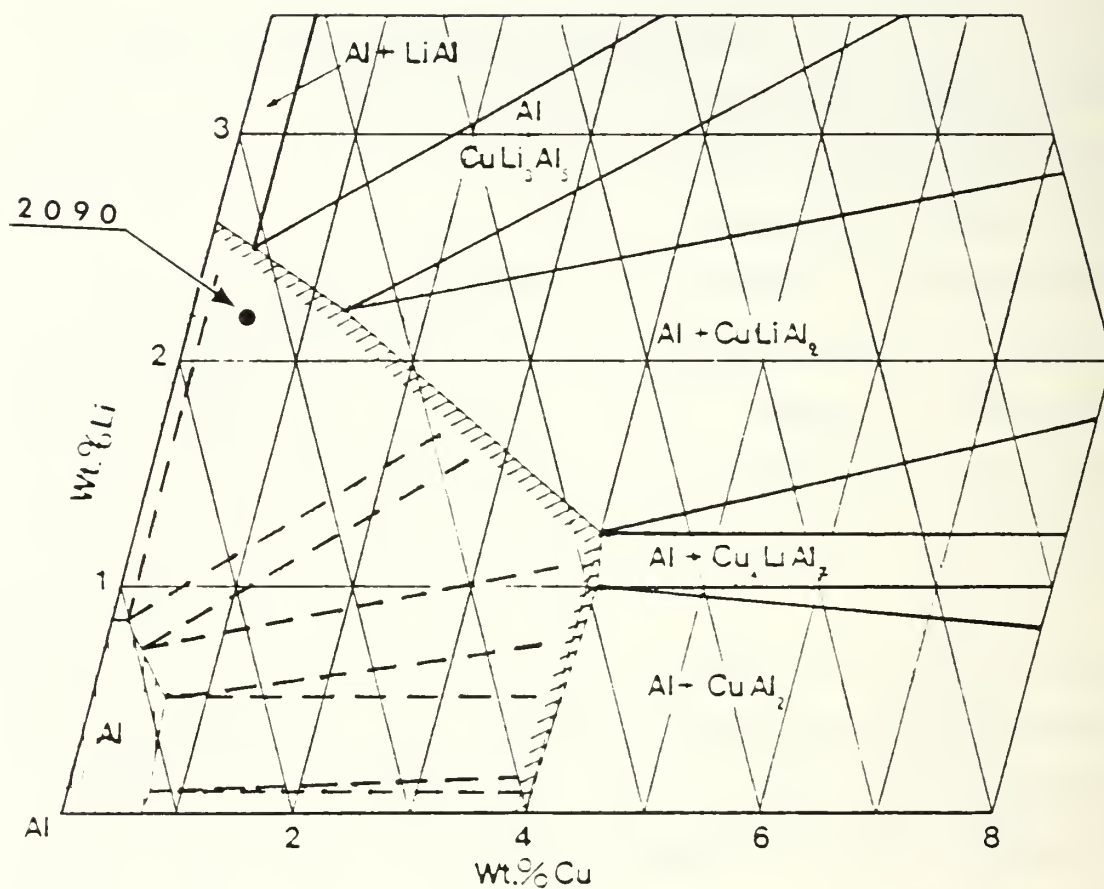
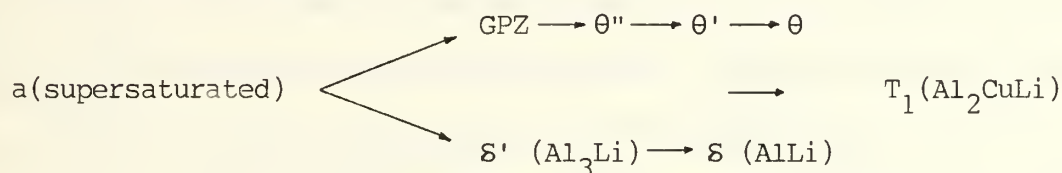


Figure 2.4. Aluminum corner of the Aluminum-Copper-Lithium Phase Diagram; phase distribution at 502°C (solid lines) and 327°C (dashed lines)

form in the Al-Cu-Li alloys [Ref. 10,11,12,13]. These phases are T_1' , T_2' , T_B' , δ' (Al_3Li), θ' (Al_2Cu), θ'' and GP zones. The T_1' and T_2' are considered to be precursors to the equilibrium T_1 and T_2 phases but their structures are still unknown.

Precipitation in the Al-Cu-Li system is complicated and Sanders [Ref. 14] has summarized the precipitation sequence as follows:



Because zirconium is present in the system, the β' phase (Al_3Zr) precipitates which exhibits a spheroidal shape, with size ranging from 100 to 300 Å, and acts to control grain growth and provide added strengthening. It is formed by a peritectic reaction and its melting point is 1577°C.

B. ALITHALITE ALLOY 2090

ALCOA's 2090 alloy is an Al-Cu-Li-Zr alloy belonging to the first generation of ALITHALITE Aluminum-Lithium alloys and has been introduced to replace the high strength 7075-T6 alloy currently used in aircraft structures.

Alloy 2090 has 7% lower density and 10% higher elastic modulus than 7075-T6. It is being produced as sheet, plate, extrusions in a T8 temper condition, and as forgings in a T6E203 condition. Alcoa registered the composition of 2090 with the Aluminum Association in

1984. The composition 2090 is listed in Table 2.1 while its physical and mechanical properties are in Tables 2.2 and 2.3 respectively [Ref. 15,16]. The fatigue resistance of 2090 and generally of all other Aluminum Lithium alloys show a significant natural improvement over the non-lithium aluminum alloys which they intend to replace. Northrop Aircraft Division has tested a sample of 2090 alloy from mill-fabricated 44mm thick plate using a tension-dominated, lower-wing load spectrum from an F/A-18A aircraft. The same spectrum of load conditions was used for testing 2024-T351, 2020-T651, 7075-T7351, 7075-T650 alloys. The results revealed an increase in fatigue life by more than a factor of five, using 2090 instead of using the other alloys which are considered to be the most resistant to fatigue crack growth.

The upgraded fatigue resistance, the density reduction and the increase of elastic modulus, which alloy 2090 provides, are properties attractive to the aerospace industry. Structural weight reduction, because of density reduction, is a very efficient means of improving aircraft performance and the increase in elastic modulus allows greater load-carrying capability in stiffness-critical aircraft components.

C. SUPERPLASTICITY

Superplasticity is the ability of some alloys to exhibit very large, neck-free tensile elongations under certain processing conditions. Common superplastic alloys exhibit elongations of 500 to 1000%, but alloys exhibiting elongation to fracture above 200% are considered superplastic. For comparison, normal materials exhibit elongations less than 100% at elevated temperatures.

Table 1
Composition of 2090, wt%

	<u>Li</u>	<u>Cu</u>	<u>Zr</u>	<u>Mg</u>	<u>Fe</u>	<u>Si</u>
Nominal	2.2	2.7	0.12	--	--	--
Minimum	1.9	2.4	0.08	--	--	--
Maximum	2.6	3.0	0.15	0.25	0.12	0.10

Table 2
Physical Properties of 2090

Density, g/cm ³	2.57
Melting Range °C	561-588
Thermal Conductivity J/([sec cm ² C]/cm	0.834-0.924
Linear Coefficient of Thermal Expansion	
20-100°C	16.2 x 10 ⁻⁶ m/m/°C
Specific Heat at 100°C	1203 (J/kg k)

Table 3
Mechanical Properties of 2090

	<u>Desired</u>	<u>Obtained*</u>
Ultimate Tensile Strength (MPa)	538-579	545
Tensile Yield Strength (MPa)	496-524	516
Compressive Yield Strength (MPa)	489-510	-
Elongation (%)	8-10	6.5
Toughness Kic (MPa m)	27.5	-
Elastic Modulus (GPa)	75.8	-

* Longitudinal direction for plate 160mm thick.

In 1934 Pearson demonstrated 1950% elongation in a Sn-Bi alloy but this result remained in the laboratory. Interest was stimulated by the review of Soviet work in this field by Underwood in 1962 [Ref. 17]. Since then there has been a tremendous scientific and commercial interest in the phenomenon so that simple superplastic forming of a wide range of commercial alloys into complex shapes is now being carried out. When superplastic forming is used, many separate parts are combined into one and formed as a monolithic structure. In this way there is a reduction in the number of parts, fasteners, costs associated with materials, fabrication, assembly, inspection, installation and in maintenance time and labor.

How does superplasticity in an alloy work? The occurrence of superplasticity depends on both the processing and the material. From the aspect of processing the material, strain rate and temperature are two critical factors for superplastic forming. In superplastic materials the flow stress is highly strain-rate sensitive. There is a characteristic sigmoidal relationship between the flow stress and strain rate plotted on logarithmic scales, Figure 2.5a [Ref. 18]. Portions of the curve of Figure 2.5a may be described by the formula:

$$\sigma = k\dot{\epsilon}^m$$

where σ is the flow stress, $\dot{\epsilon}$ is the strain rate, k is the material constant that depends upon test temperature, the microstructure and defect structure of the specimen and m is the strain-rate sensitivity coefficient.

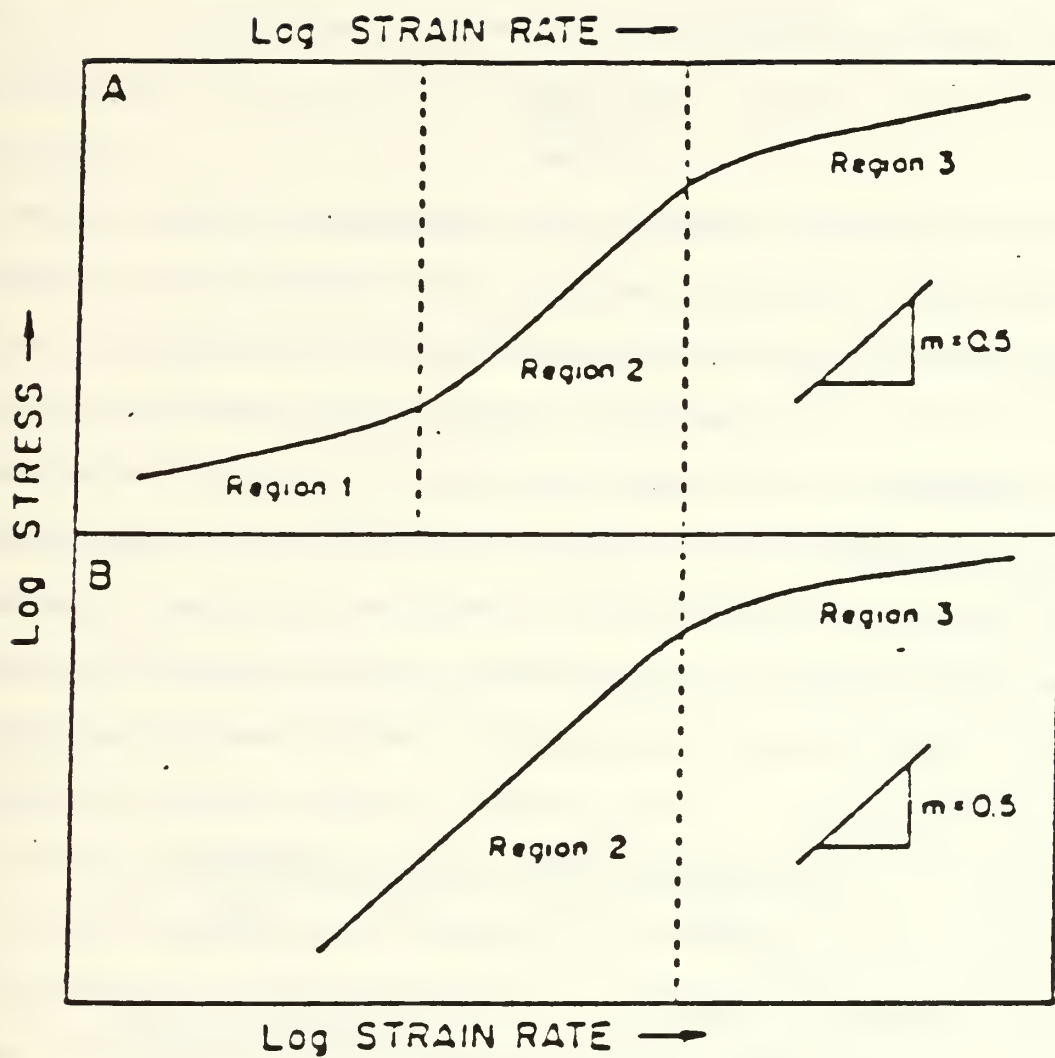


Figure 2.5. Stress versus Strain Rate. Shape of curves that different materials exhibit during Superplastic deformation

The strain-rate sensitivity coefficient, m , describes the capacity of the material to resist necking and has been used as a criterion to assess proposed mechanisms of superplastic deformation. Frequently in the literature m is reported as the slope of the $\ln\sigma$ versus $\ln\dot{\epsilon}$ curve, Figure 2.5 and is defined as:

$$m = \frac{d[\ln\sigma]}{d[\ln\dot{\epsilon}]}$$

For many superplastic materials, the sigmoidal curve is divided into three regions. In regions 1 and 3, at low and high strain rates respectively, m is less than 0.3 but in region 2, m is greater than 0.3 and this region is the superplastic region where large elongations occur. Superplastic alloys generally have m values near to 0.5 and optimum strain-rates for this between 10^{-4} and 10^{-2} s^{-1} . The stress versus strain rate relation and m value in particular depend on deformation mechanisms in turn determined by the microstructure of the material. It is widely recognized [Ref. 18,19] that the principle deformation mechanism in superplasticity is grain boundary sliding accommodated by either climb-controlled slip or diffusional processes.

Because of this requirement for diffusion, the phenomenon is seen at elevated temperatures, usually 0.4 to 0.7 T_m where T_m is the melting temperature. A fine grain size will minimize diffusion distances and thereby facilitate the grain boundary sliding and superplastic response. The grain boundaries are thought to be sinks and sources for vacancies in superplastic flow and thus high-angle boundaries are also a prerequisite in addition to fine and equiaxed grains to enhance the

sliding. It is often seen that the strain rate $\dot{\epsilon} \sim d^{-p}$, where d is the grain size and $p = 2$ or 3 . Thus a fine grain size will enhance superplasticity if the boundaries also are of high-angle character. Usually, grain size in the range of $2-5 \mu\text{m}$ is necessary to achieve superplastic response and this requires the presence of a second phase to stabilize the grains and retard their growth at elevated temperatures.

Several physical models have been used to derive constitutive equations for high temperature deformation, taking into account grain boundary sliding, diffusional creep and dislocation creep mechanisms as well as several other deformation mechanisms which contribute to superplasticity. Most of the theories are not entirely adequate. A model proposed by Ashby and Verrall assumes that the rate of grain boundary sliding is limited by the rate of the process providing accommodation strains at grain boundary triple junctions, which they consider to occur by diffusion. The proposed equation is the following [Ref. 20]:

$$\dot{\epsilon} = \underbrace{\frac{100\Omega D_v}{\kappa T d^2} \left[\delta - \frac{0.72\Gamma}{d} \right]}_{\text{grain boundary sliding}} \underbrace{\left[1 + \frac{3.3\delta D_b}{d D_v} \right]}_{\text{diffusional creep}} + \underbrace{\frac{A D_v G b}{K T} \left[\frac{\delta}{G} \right]^n}_{\text{dislocation creep}}$$

where $\dot{\epsilon}$ is the strain rate, σ is the applied stress, Ω is the atomic volume, b is the Burger's vector, d is the grain size, S is the grain boundary width, D_b is the bulk diffusivity, D_v is the grain boundary diffusivity, Γ is the grain boundary energy, G is the shear modulus, n, A

are the constants, k is the Boltzmann constant and T is the temperature. The above equation can be used to describe deformation in single and quasi-single phase alloys, but for more complex alloys further assumptions and qualifications are needed. Although there is not a completely accurate physical model to describe superplasticity, the existing models can be used to identify the primary material parameters that control the strain-rate and temperature ranges where extensive superplasticity occurs.

D. PREVIOUS INVESTIGATIONS AT NPS

Previous work at the Naval Postgraduate School has centered on the Al-Mg-X system and through specific thermomechanical processes superplastic response of the material has been attained. In Aluminum Magnesium alloys the material is homogenized and then comes to a temperature where concurrent precipitation of the intermetallic β phase (AlMg_5), while working the material, takes place. The objective in the microstructural sense is to achieve an interaction between the dislocation structures and the precipitating particles. The intermetallic needs to be moderately coarse, 0.5 to 1.0 μm . In order to interact with and stabilize the microstructure. If it is coarser, 2 to 3 μm it seems that these particles promote discontinuous recrystallization and a resultant coarse microstructure which is not superplastic. It has been demonstrated by Hales and McNelley [Ref. 21] that the dislocation structures produced by such processing recover to form boundaries of 2° - 7° misorientation. The superplastic response,

even at such small misorientation, suggests these boundaries to be of sufficient misorientation to sustain superplastic flow processes.

E. OBJECTIVE OF THIS RESEARCH

The objective of this research is to investigate the applicability of the thermomechanical processing developed at NPS for other materials, including Aluminum-Magnesium and Aluminum-Magnesium-Lithium alloys, to the alloy 2090.

Previous attempts to make the 2090 alloy superplastic have centered around thermomechanical processing to produce a fine grain size. In order to accomplish this goal the primary objective has been a redistribution of the T_1 phase which tends to precipitate on grain boundaries during conventional processing. Uniform distribution of fine T_1 precipitates has been achieved by a combination of cold working and aging treatments. In this manner a reasonably fine grain size of the order of $20\mu\text{m}$ has been attained, which corresponds to the interparticle spacing of the T_1 phase in the microstructure. Transformation of the structure is considered to be by a discontinuous recrystallization mechanism involving nucleation and growth of new strain-free grains.

The objective of research at NPS is to use the same methods, involving cold rolling and aging, to produce the desired distribution of T_1 phase. Subsequent processing however differs from previous work in that controlled warm rolling is utilized instead of recrystallization heat treatments. The resultant microstructure is in an essentially non-recrystallized condition.

It is hoped that the 2090 alloy will undergo similar microstructural changes to the Al-Mg-Li-Zr alloys studies at NPS, such that a fine-grained structure will develop from the as-rolled structure via a continuous recrystallization mechanism both during reheats between rolling passes and concurrently with elevated temperature testing. Continuous recrystallization is characterized by the development of a new strain-free microstructure in the absence of nucleation and growth mechanisms and may result in grains 2-5 μ m in size.

III. EXPERIMENTAL PROCEDURE

A. MATERIAL

The alloy 2090-T8A41 studied in this research was fabricated by ALCOA. The as received material was a plate with dimensions about 51 x 31 x 4 cm (L x W x T) heat treated to a T8 temper (solution heat-treated, cold worked and then artificially aged) [Ref. 22], and anodically coated in a A41 type of coating (architectural class I) [Ref. 23].

Three specimens of size 12.7 x 4.8 x 4.8 mm, each from a different corner of the plate, were prepared and sent to ANAMET Laboratories Inc. for chemical analysis. Analysis was performed using atomic absorption (Cu,Li), and X-ray (Zr) techniques. The results of this analysis [Ref. 24] reveal only slight differences in composition for Cu and Li and values are within the specified composition limits. The data are shown in Table 4.

Table 4
Sample Composition

	<u>Cu</u>	<u>Li</u>	<u>Zr</u>
1	2.52	2.01	0.12
2	2.60	2.03	0.12
3	2.56	2.04	0.12
Average	2.56	2.03	0.12
Nominal	2.70	2.20	0.12

B. THERMOMECHANICAL PROCESSING

Billets of dimensions about 41 x 43 x 51 mm were sectioned from the plate. They were thermomechanically processed using an initial cold

working and lower temperature aging treatment followed by warm rolling. Figure 3.1 is a schematic illustration of the essential TMP used. The actual processes are tabulated in Table 5, and involve various cold working and aging treatments in combination with various warm rolling procedures to investigate process effects on microstructure and properties.

1. Solution Treatment and Upset Forging

Solution treatment is intended to produce uniform starting condition by dissolving the soluble precipitates, placing in solution Li and Cu alloying elements. The β' phase (Al_3Zr) particles are insoluble at temperature below the melting range of the alloy.

Table 5
Thermomechanical Processing Schedule

TMP	Aging Time (hrs)	Reheating Time Per Pass (min)	Final Rolling Strain	Reduction Per Pass (mm)
1	0	4	2.4	2.5
2	4	4	2.4	2.5
3	16	4	2.4	2.5
4	0	30	2.4	2.5
6	4	30	2.4	2.5
7	16	30	2.4	2.5

Solution treatment was performed at 540°C to ensure a temperature well in excess of the solvus, which for Li is 400°C and for Cu is 450°C based on the binary diagrams. Time duration was two hours total heating time of the material.

Hot working, intended further to refine and homogenize the solution treated material, was conducted at 480°C . This was accomplished by upset forging on heated platens. The TMP conditions are

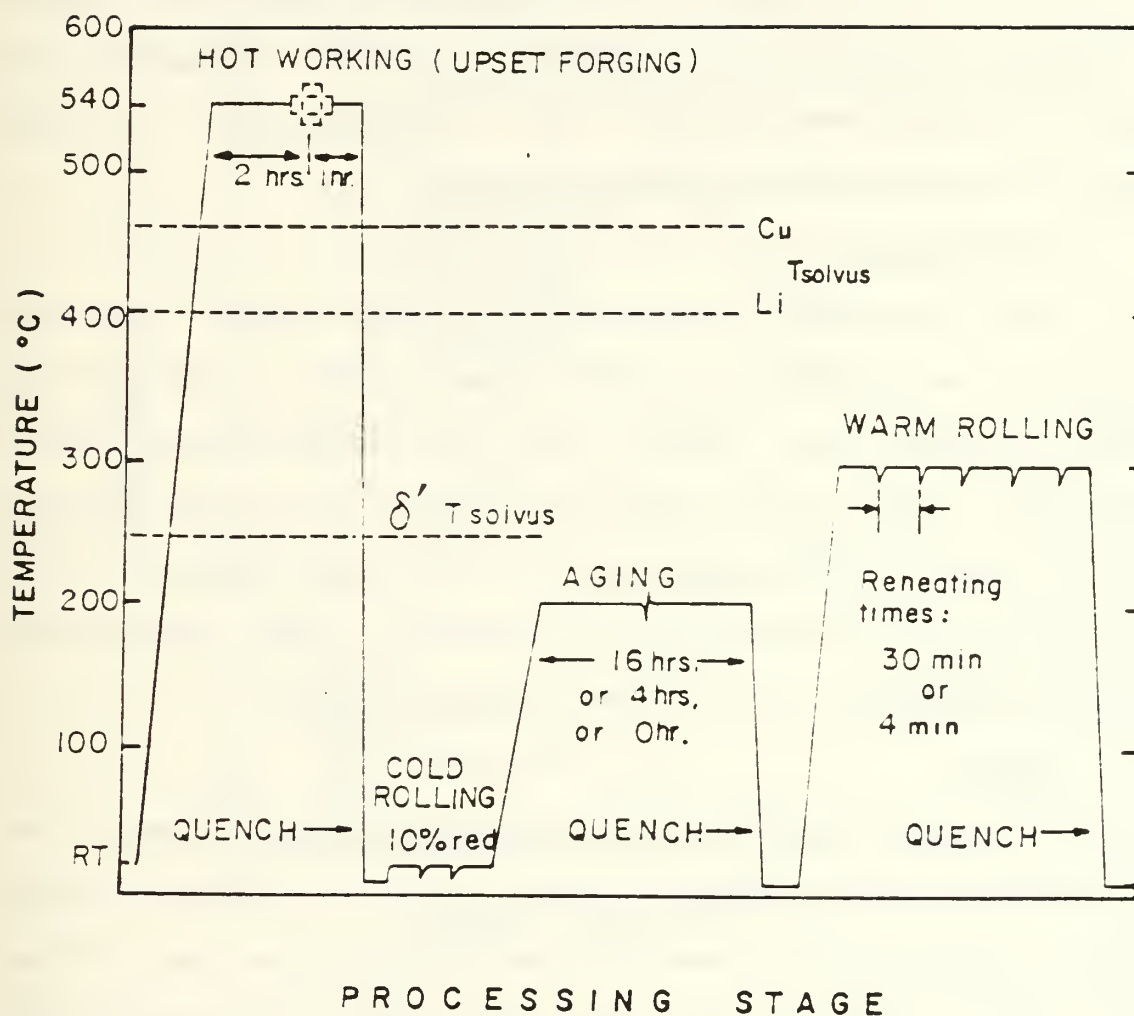


Figure 3.1. Thermomechanical Processing Techniques

indicated on a partial Aluminum-Lithium phase diagram shown in Figure 3.2. The billets were upset along their greatest dimension, which was parallel to the rolling direction of the plate, from 50.8 mm height to 25.4 mm thickness. Non uniform deformation after upset forging was noted, revealing the presence of texture in the material.

At the conclusion of the hot working, the billets were reheated for one hour to ensure that the subsequent quenching temperature was above the solvus, and then cold water quenching (about 10°C) was employed to avoid precipitation during cooling.

2. Cold Working

The introduction of dislocations during rolling at room temperature was designed to provide nucleation sites for precipitating phases, increasing their number and the homogeneity of their distribution. Each forged billet was sectioned in two pieces and each piece was rolled in a direction parallel to the longest dimension of the piece. From an initial thickness of 25.4 mm to a final thickness of 22.86 mm corresponded to a total reduction of 10 percent.

3. Aging

Artificial aging was designed to produce a uniform dispersion of a fine, hard precipitate in a softer matrix. The selected aging temperature for the billets was 200°C and the aging times were either zero, four or sixteen hours. After aging cold water quenching was employed into water at a temperature of about 10°C.

4. Warm Working

The warm working temperature range is considered to be between 200°C and the solvus of the alloy [Ref. 25]. The billets were heated

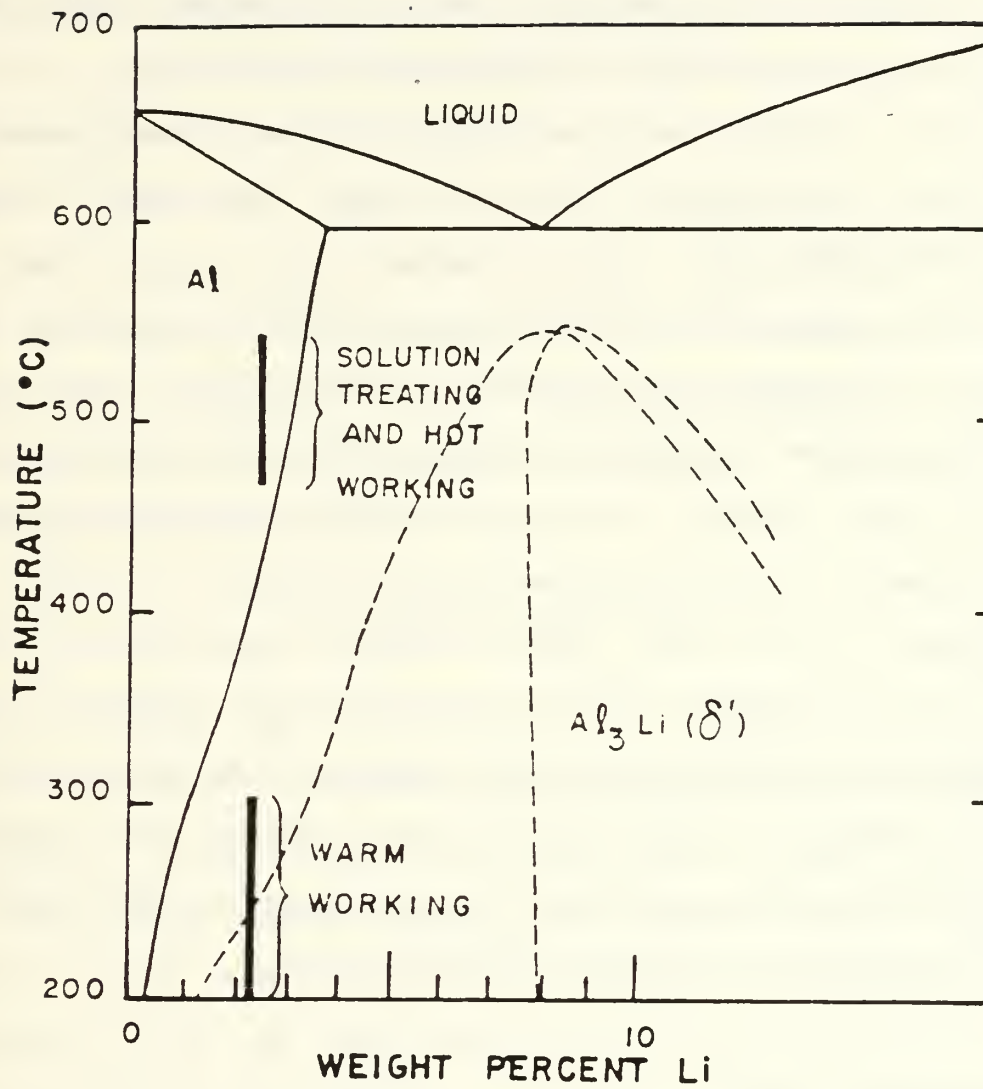


Figure 3.2. Partial Aluminum-Lithium Phase Diagram with TMP regions indicated

from room temperature to 300°C, with a 30 minute total preheating time and then rolled to completion followed by cold water quenching at 10°C. To maintain the isothermal conditions indicated on Figure 3.1 the billets were reheated between each pass. Two reheating times between each rolling pass were used, four minutes and thirty minutes.

The reduction per pass during rolling was 2.5 mm corresponding to thickness reduction of 11 percent the first and about 55 percent during the final pass. Final thickness was 2.0 and thus total warm rolling true strain was 2.4. Defects introduced into the alloy during this step are essential for continuous recrystallization. Warm rolling also creates zones of intense deformation around the hard precipitates.

Initial attempts to warm roll a billet, aged 16 hrs in initial heat treatment, followed by preheating for 1 hour prior to rolling were unsuccessful. This billet cracked severely during the first rolling pass. It is believed that the preheating time allowed excessive precipitation and coarsening of a grain boundary phase. Thus preheating time was reduced to 30 minutes and no further problems were encountered. The rolling procedure resulted in a double bulging [Ref. 26] of the edge with no alligatoring or center splitting occurring.

C. MECHANICAL TESTING

After warm rolling the final sheet thickness was 2 mm. The rolled sheets were then cut into specimen blanks, to the dimensions given by Wise [Ref. 26: pp.31], maintaining the rolling direction as the

longitudinal dimension. Elevated temperature testing was conducted using an electromechanical Instron machine. A Marshall Model 2232 three-zone clamshell furnace mounted on the test machine was used to conduct elevated temperature testing at temperatures of 300, 370, 440 and 510°C. The crosshead speeds used were 0.05, 0.5, 5, 50, and 127 mm/min corresponding to nominal strain rates of 6.67×10^{-5} , 6.67×10^{-3} , 6.67×10^{-2} and $6.67 \times 10^{-1} \text{ s}^{-1}$ respectively. The chart speeds used were 5 mm/min for the first two crossheads speed and 50, 508, and 1270 mm/min for the remaining three speeds respectively. The conditions used for tensile testing are summarized in Table 6.

Actual elongation was determined by measuring the marked gage section before and after testing. Then

$$\% \text{ Elongation} = \frac{L_f - L_o}{L_o} \times 100$$

where L_f is the final length and L_o the initial length of the gage section. The Instron strip chart gives the applied force (lbs) versus chart motion. A "floating slope" was used to take raw data from the strip chart, making corrections for such factors as grip slippage, elasticity of the sample and Instron components themselves. The magnification ratio and correction factor used for data reduction are given by the following formulas:

$$\text{Magnification Ratio} = \frac{c}{x}$$

where c is the chart speed and x is the crosshead speed;

$$\text{Correction Factor} = \frac{\text{Actual Elongation}}{\text{Measured Elongation}}$$

where Actual Elongation = $L_f - L_o$ and Measured Elongation = Horizontal distance between "floating slope" and point of zero load on curve from strip chart, divided by Magnification Ratio.

Table 6
Conditions Used for Tensile Testing

<u>T = 300°C</u>				
Strain rate	TMP 1	TMP 2	TMP 6	TMP 7
6.67×10^{-5}	1	2	3	4
6.67×10^{-4}	5	6	7	8
6.67×10^{-3}	9	10	11	12
6.67×10^{-2}	13	14	15	16
1.67×10^{-1}	17	18	19	20
<u>T = 370°C</u>				
6.67×10^{-4}		21	22	
<u>T = 440°C</u>				
6.67×10^{-4}		23	24	
<u>T = 510°C</u>				
6.67×10^{-4}		25	26	

Additional equations used for data reduction are as follows:

$$S = \text{Engineering Stress} = \frac{P}{A_o}$$

where P is the load and A_o is the cross sectional area;

$$e = \text{Engineering Strain} = \frac{L_f - L_o}{L_o}$$

$$\epsilon = \text{True Strain} = \ln(1+e)$$

$$\sigma = \text{True Stress} = S(1+e)$$

All raw data was analyzed using a computer program, a copy of which

is included in Appendix A. All reduced data was used for further generation of graphics using the Easyplot Program.

D. METALOGRAPHY

In support of this research both optical microscopy (OM) and transmission electron microscopy (TEM) were carried out. In order to study grain shape and size as well as the second phase shape, size and distribution, specimens from all stages of the thermomechanical processing and the as-rolled condition were examined by OM.

The specimens were first cold mounted in an acrylic compound and then polished by wet silicon carbide abrasive papers following a sequence of 240, 320, 400 and 600 grit. After the rough polishing, diamond paste followed by final polishing with magnesium oxide was accomplished. All the examined optical micrographs were obtained after etching for 45 to 90 seconds in Graff-Sargent etchant followed by 8-14 seconds in Keller's etchant [Ref. 27:pp. 354]. Metallographic examination was conducted with a ZEISS ICM 405 optical microscope.

TEM specimens were examined from as-rolled and tensile tested material processed with TMP 2 and TMP 6. Blanks 3 mm in diameter and 0.25 mm thick were punched from bulk material with the foil normal parallel to the rolling plane normal. The specimens were prepared for TEM in the conventional manner using a STRUERS TENUPOL. Operating conditions consisted of an electrolyte of 25% Nitric acid in methanol at -15°C to -20°C with an applied voltage of 15 volts which produced a current of approximately 0.3 A. TEM was conducted on a JEOL 120 CX operating at a voltage of 120 KV.

IV. RESULTS AND DISCUSSION

This chapter will examine the effect of the thermomechanical processing variables on microstructural development and mechanical behavior of 2090 alloy. Recent research on Al-Mg alloys has demonstrated that increased reheating time between warm rolling passes facilitates continuous recrystallization. This resulted in enhanced superplastic response during subsequent mechanical testing. Particular attention was given here to examination of the effect of reheating time on microstructure development and also mechanical properties.

A. EFFECT OF PROCESSING ON MICROSTRUCTURE

1. Optical Microscopy Results

Optical microscopy examination revealed a structure consisting of elongated grains, with second phase precipitation in grain interiors as well as on grain boundaries. The degree of non-uniformity of precipitates depended on the TMP employed, especially upon the reheating time.

a. Aging Time Effect

The prior cold work/aging treatment was intended to initiate precipitation in grain interiors. The longer aging times were expected to produce more extensive precipitation and to result in more uniform structure following TMP. However, little or no difference attributable to prior aging treatments was discernible. This may be seen in examination of the optical micrographs, Figures 4.1, 4.3, 4.5 for

material aged for 0, 4 and 16 hrs, respectively. Similarly, the optical micrographs in Figures 4.2, 4.4, 4.6 are for material aged for 0, 4 and 16 hrs respectively, but reheated for longer times between passes during the subsequent rolling. Intergranular precipitation was seen in all samples rolled with four minutes reheating, irrespective of prior aging time. Precipitation was more uniform in material reheated 30 minutes, between passes for all aging treatments.

b. Reheating Time Effect

Comparing the microstructure of those TMPs where only the reheating time between warm rolling passes is changed, a significant difference is evident in the microstructure. Comparing TMP1 (4 mins. reheating time) in Figure 4.1 with TMP 4 (30 mins.) in Figure 4.2, it is clear that the longer reheating time results in a more uniform distribution of the second phase precipitates while the short reheating time maintains the boundary-decorated grain structure. The same conclusion is reached by comparison of TMP 2 in Figure 4.3 with TMP 6 in Figure 4.4, and TMP 3 in Figure 4.5 with TMP 7 in Figure 4.6.

A detailed explanation for this effect cannot be offered. It is likely that the initial cold working and aging precipitates relatively little of the available Cu and Li. Most of these components are then available to precipitate in the subsequent warm rolling. The longer reheating interval may result in a more uniform dislocation substructure, with better defined subgrains because of more time for recovery. The precipitating phase may then be able form at nodes in the

(a)

50 μm

(b)

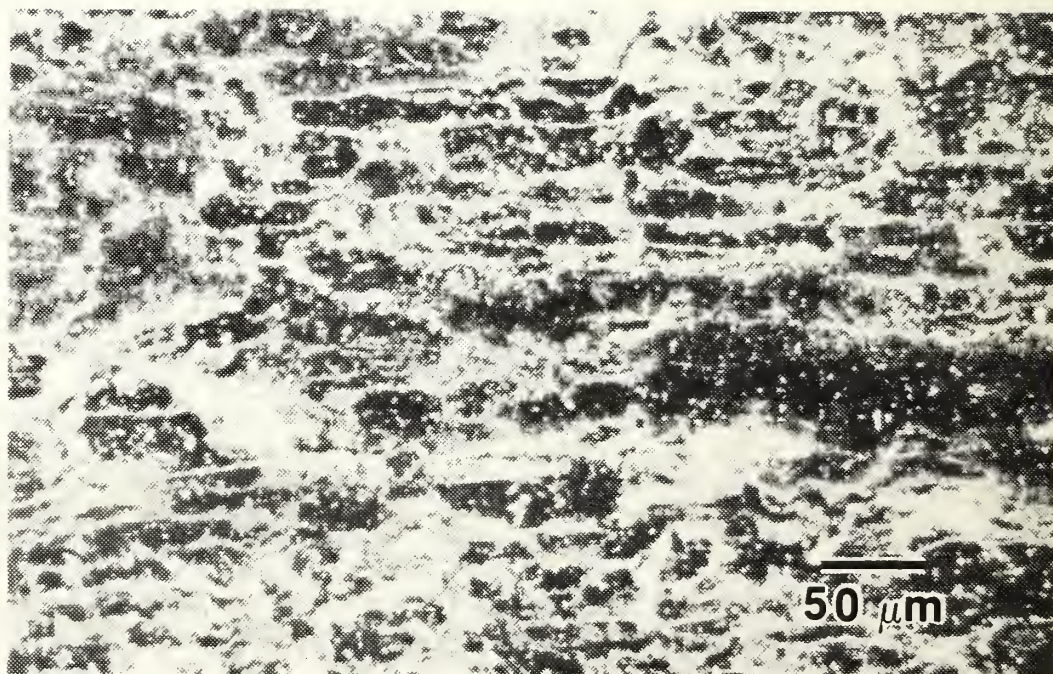
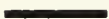


Figure 4.1. Optical micrographs, (a) bright field, (b) dark field, of alloy 2090 in the as-rolled condition processed by TMP1.

(a)


50 μm

(b)

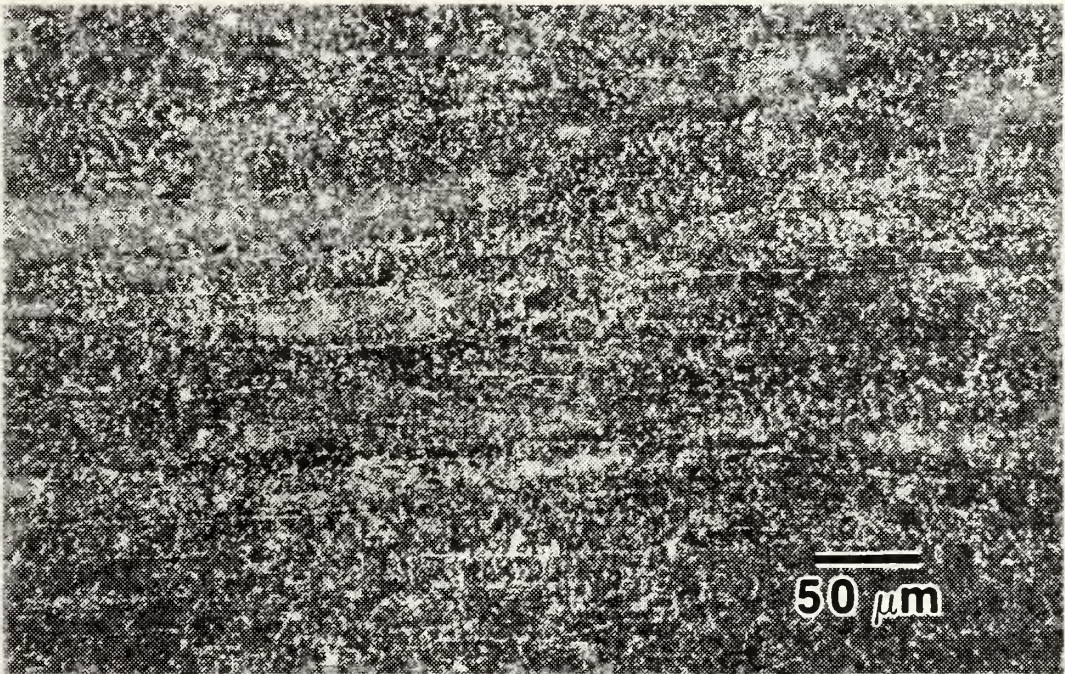



Figure 4.2. Optical micrographs, (a) bright field, (b) dark field, of alloy 2090 in the as-rolled condition processed by TMP 4.

(a)


50 μm

(b)

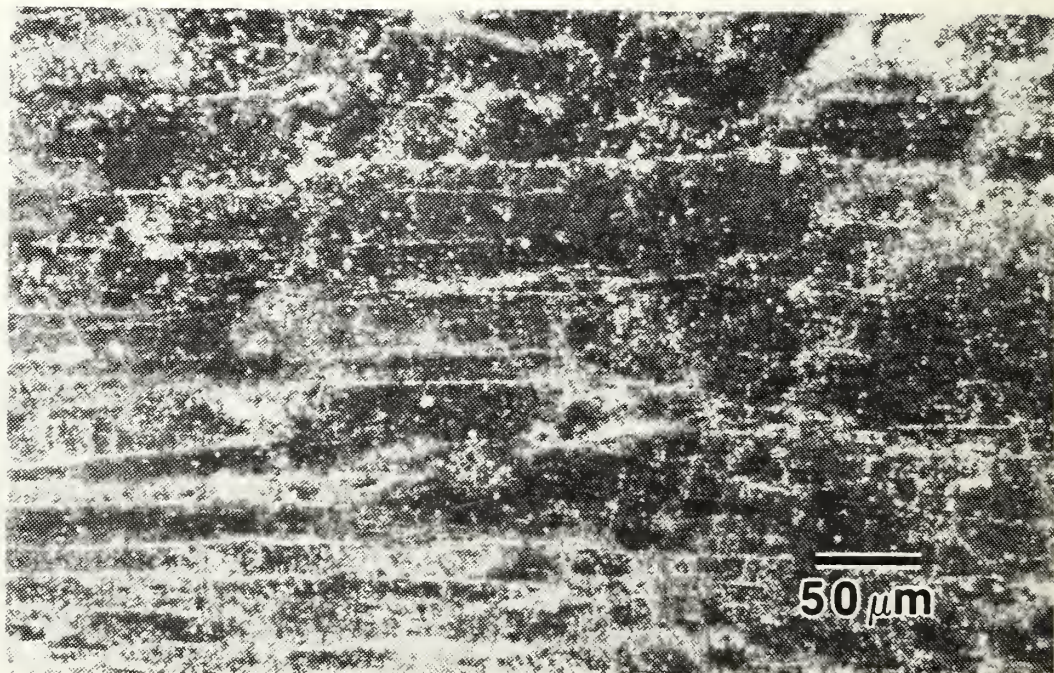


Figure 4.3. Optical micrographs, (a) bright field, (b) dark field, of alloy 2090 in the as-rolled condition processed by TMP 2.

(a)

50 μm

(b)

50 μm

Figure 4.4. Optical micrographs, (a) bright field, (b) dark field, of alloy 2090 in the as-rolled condition processed by TMP 6.

(a)

50 μm

(b)

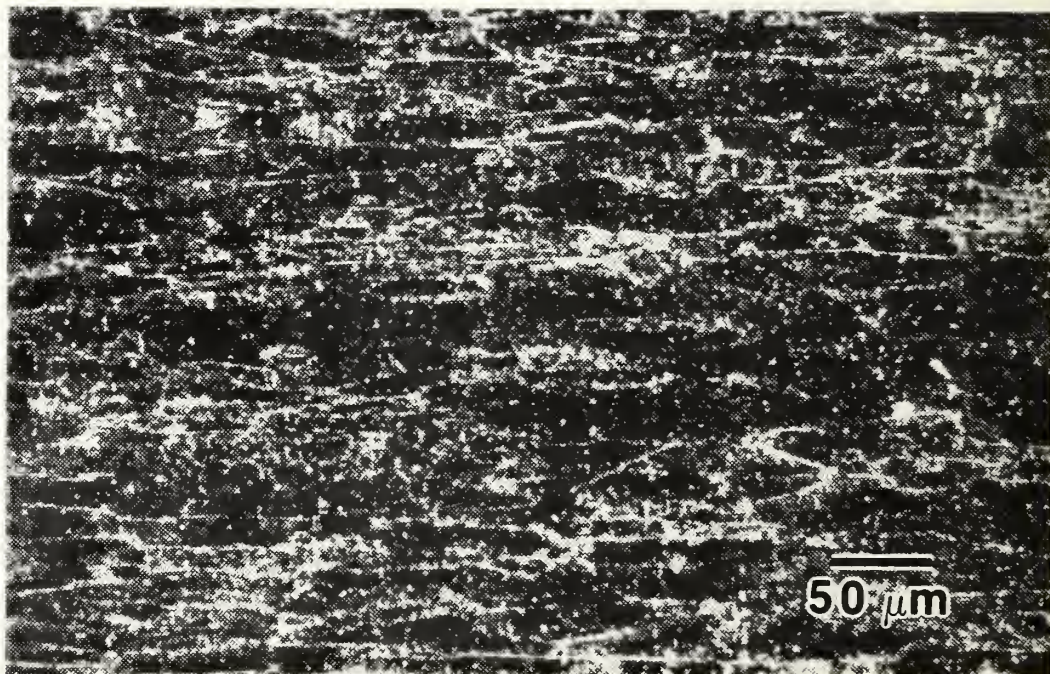
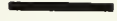


Figure 4.5. Optical micrographs, (a) bright field, (b) dark field, of alloy 2090 in the as-rolled condition processed by TMP 3.

(a)


50 μm

(b)

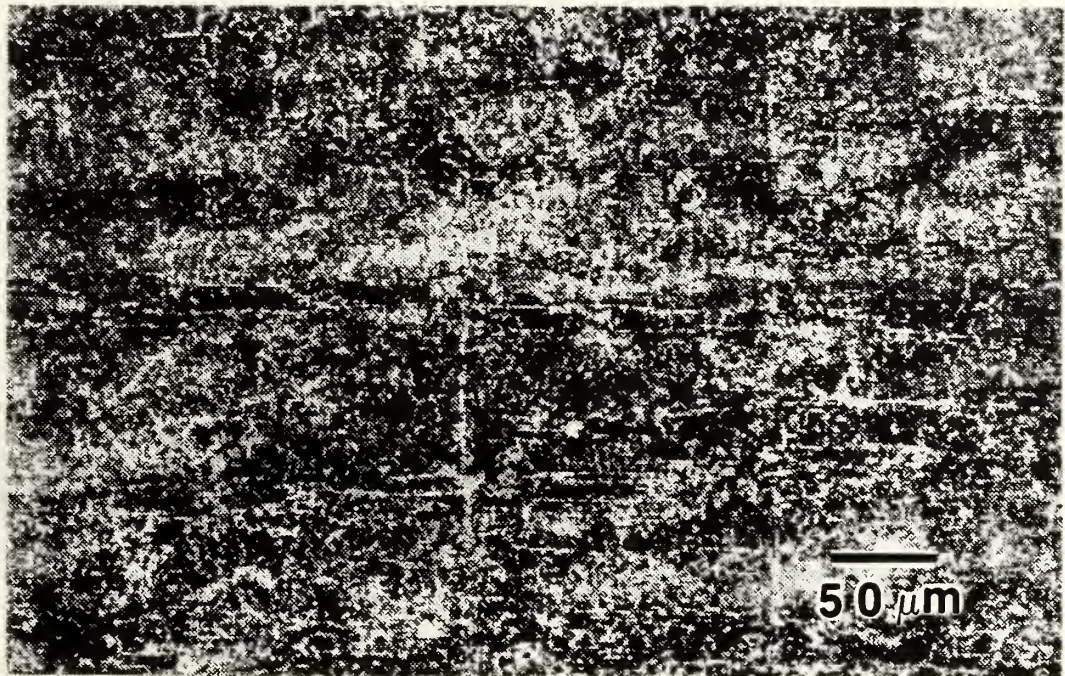


Figure 4.6. Optical micrographs, (a) bright field, (b) dark field, of alloy 2090 in the as-rolled condition processed by TMP 7.

structure and thus becomes more uniformly distributed. Some data on this was obtained by TEM to clarify this point.

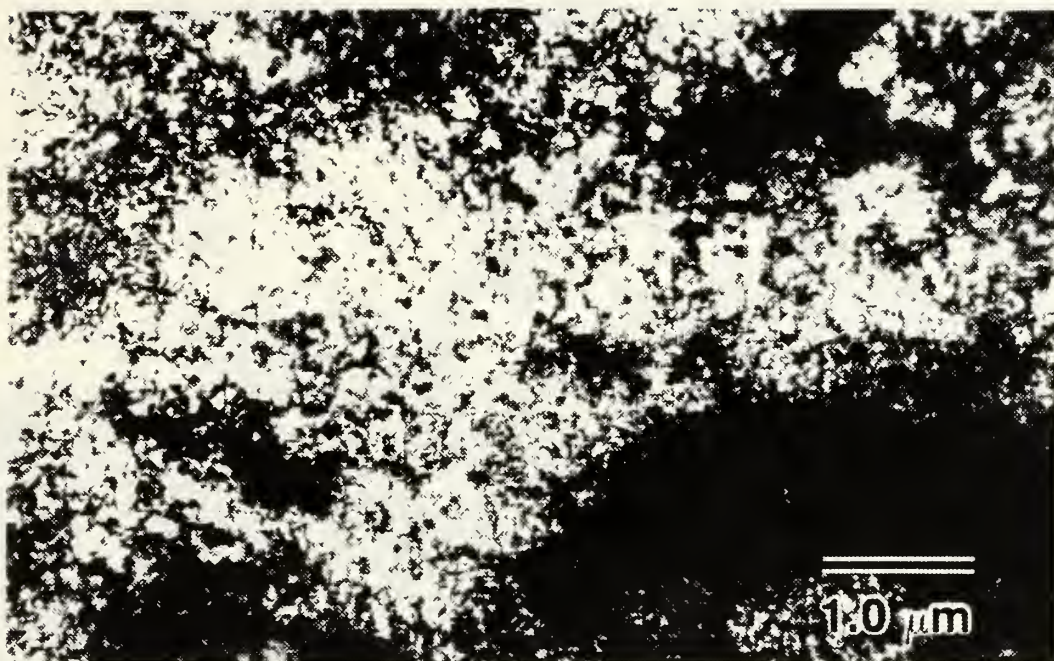
2. Transmission Electron Microscopy Results

The microstructure of alloy 2090 may contain numerous phases and is expected to be more complicated than that seen in the Al-Mg alloys. TEM revealed the existence of numerous second phase precipitates of different shapes, sizes and spacing. The detailed identification of each of these second phases is beyond the scope of this research. Transmission electron microscopy was conducted on specimens from TMP 2 and TMP 6, with 4 or 30 minutes reheating time during warm rolling respectively. Otherwise, processing was identical. These conditions were examined to gain further insight into effect of reheating time.

a. As Rolled Microstructure

Only slight differences in the structure can be seen between the two rolling conditions. In both cases a high dislocation density is evident. Comparison by TEM of TMP 2, Figures 4.7 and 4.8, with TMP 6, shown in Figures 4.9 and 4.10, reveals a higher dislocation density in TMP 2; on the other hand, there is a better-defined substructure with greater degree of recovery and precipitation in TMP 6. These results support the optical microscopy observations and suggest that the straining at warm temperature, and specifically the reheating time between rolling passes, is more important in control of the homogeneity of precipitate distribution than is the initial aging treatment. The TEM study also demonstrates that the longer reheating interval does result in enhancement of recovery in this alloy. No attempt, however,

(a)



(b)

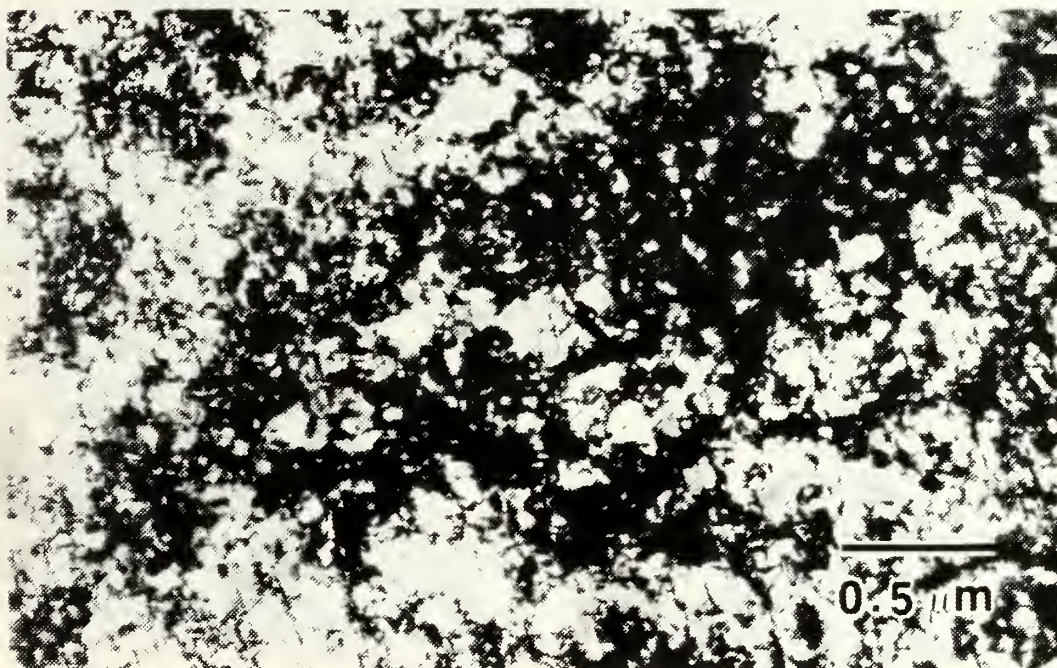


Figure 4.7. Bright field TEM micrographs, of alloy 2090 in the as-rolled condition processed by TMP 2.

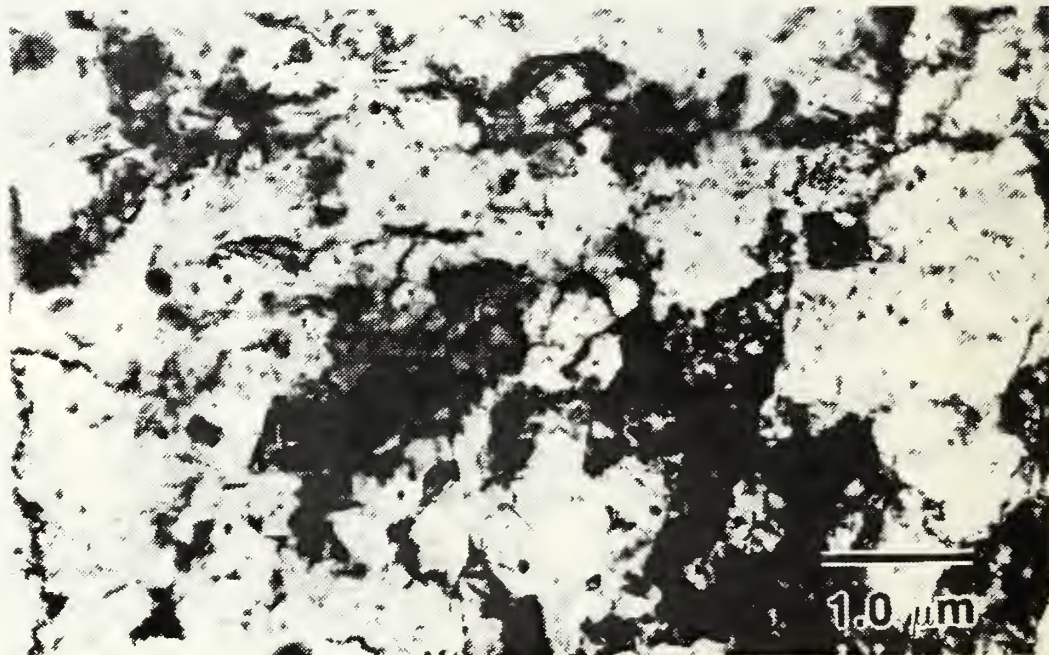
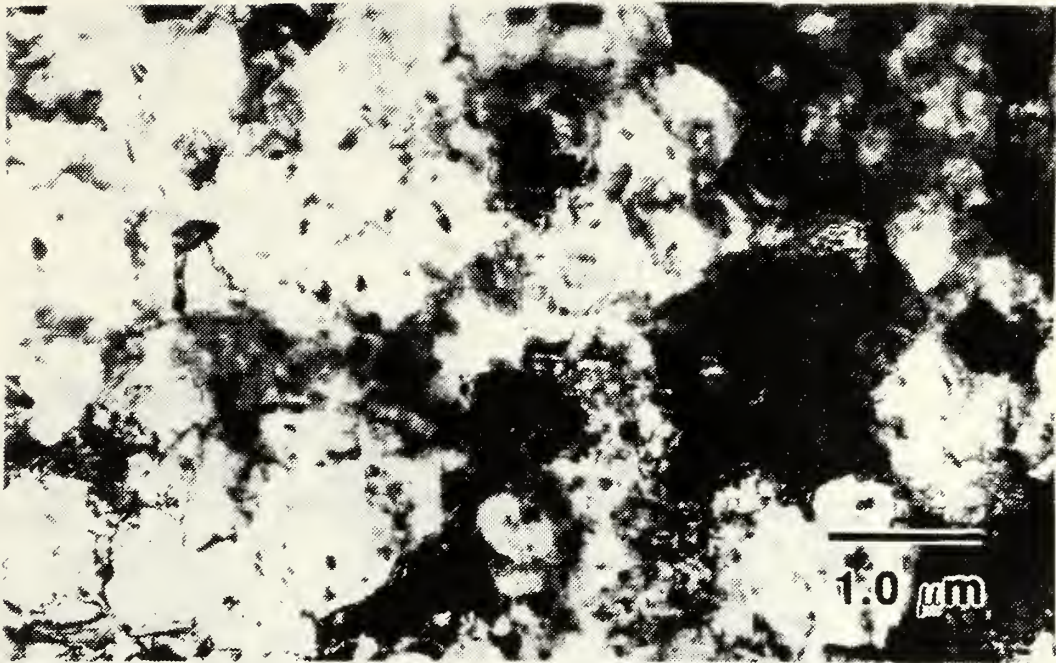


Figure 4.8. Bright field TEM micrograph of alloy 2090 in the as-rolled condition processed by TMP 2.

(a)



(b)

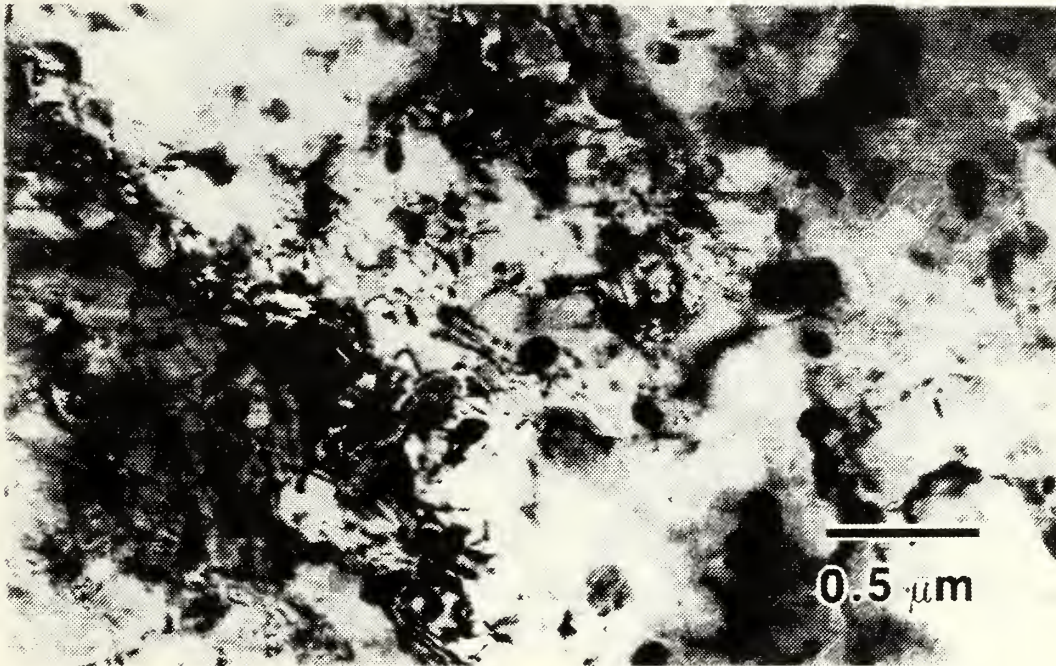


Figure 4.9. Bright field TEM micrographs, of alloy 2090 in the as-rolled condition processed by TMP 6.



Figure 4.10. Bright field TEM micrograph, of alloy 2090 in the as-rolled condition processed by TMP 6.

was made here to evaluate misorientation of the boundaries, as done previously for Al-Mg alloys [Ref. 28].

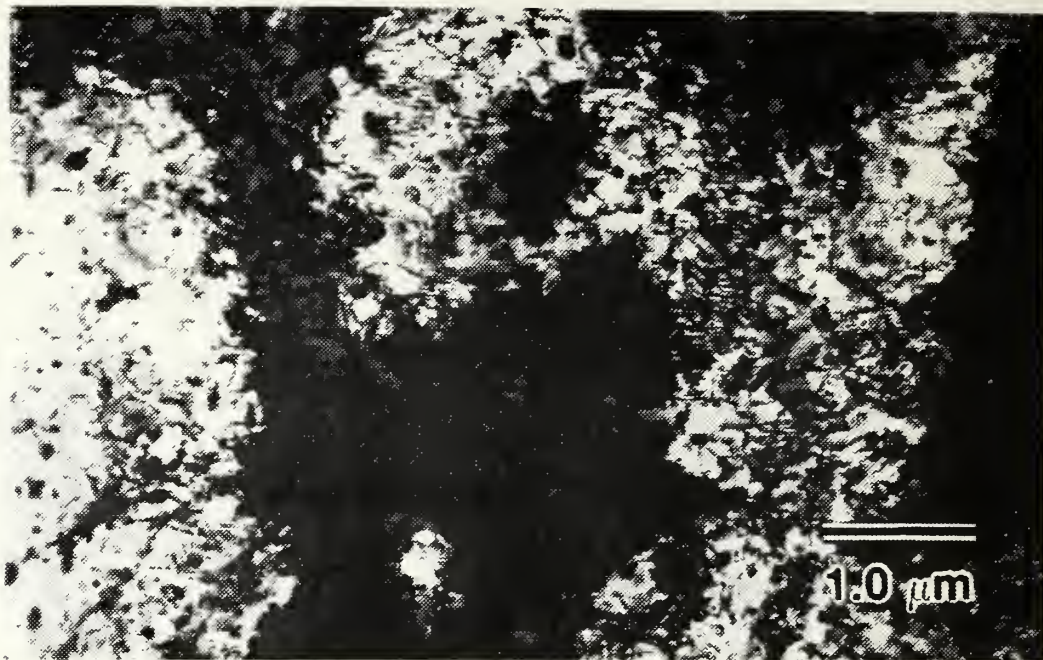
b. Effect of Heating at 300°C

The warm rolling was done at 300°C following the work done on the Al-Mg and Al-Mg-Li alloys. Also, highly refined microstructures have been shown to evolve in the Al-Mg and Al-Mg-Li alloys by continuous recrystallization [Ref. 28]. A similar investigation was done here; materials used were taken from the grip section of elevated temperature test samples. The grip sections experienced heating only and thus illustrate the effect of time at temperature. The corresponding gage sections then may be used to isolate the effect of deformation. Upon heating to 300°C both structures recover further. Figures 4.11 and 4.12, for TMP 2, show some recovery of the material but even so, the structure is not well developed and remains more like that of the as-rolled material shown previously in Figure 4.7, with relatively high dislocation density.

Second phase precipitates still decorate prior grain boundaries with a uniform distribution present inside the grains. A continuously recrystallized grain structure has not been achieved as the microstructure still consists of primarily a subgrain structure. The intragranular, plate like precipitate observed in Figure 4.11b may be the T_1 (LiCuAl_2) phase according to descriptions given by Yoshida and coworkers [Ref. 29] and Lee and coworkers [Ref. 30].

Recovery and substructure formation is much more clear in TMP 6. At longer reheating time, and when examined at higher

(a)



(b)



Figure 4.11. Bright field TEM micrographs, Of alloy 2090 from the grip section of a tensile sample tested at 300°C and $1.67 \times 10^{-1} \text{ S}^{-1}$ strain rate processed by TMP 2.

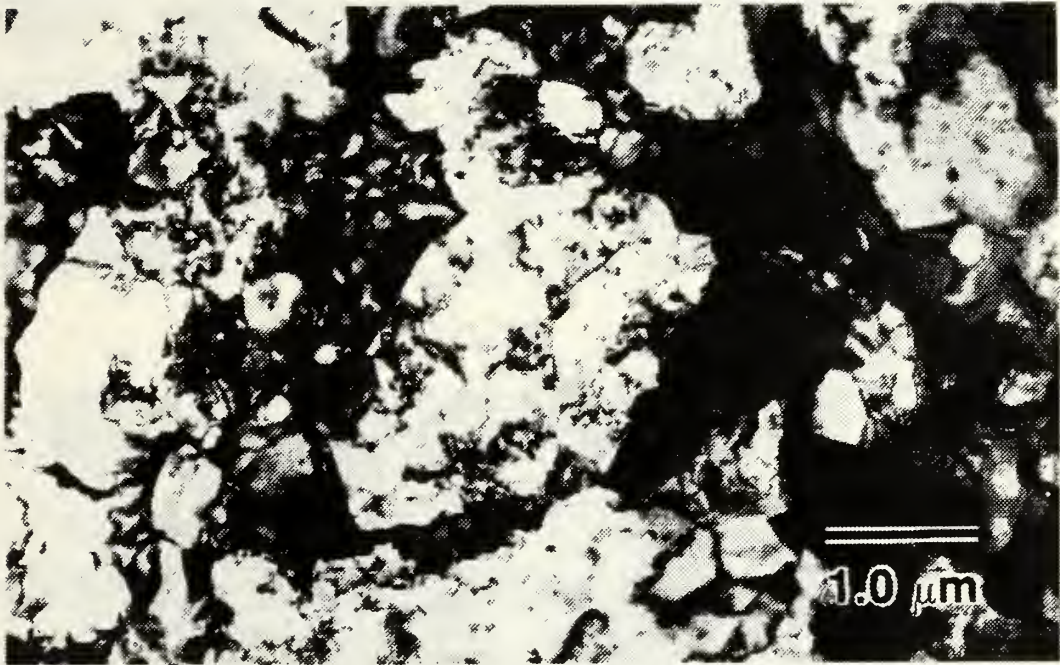


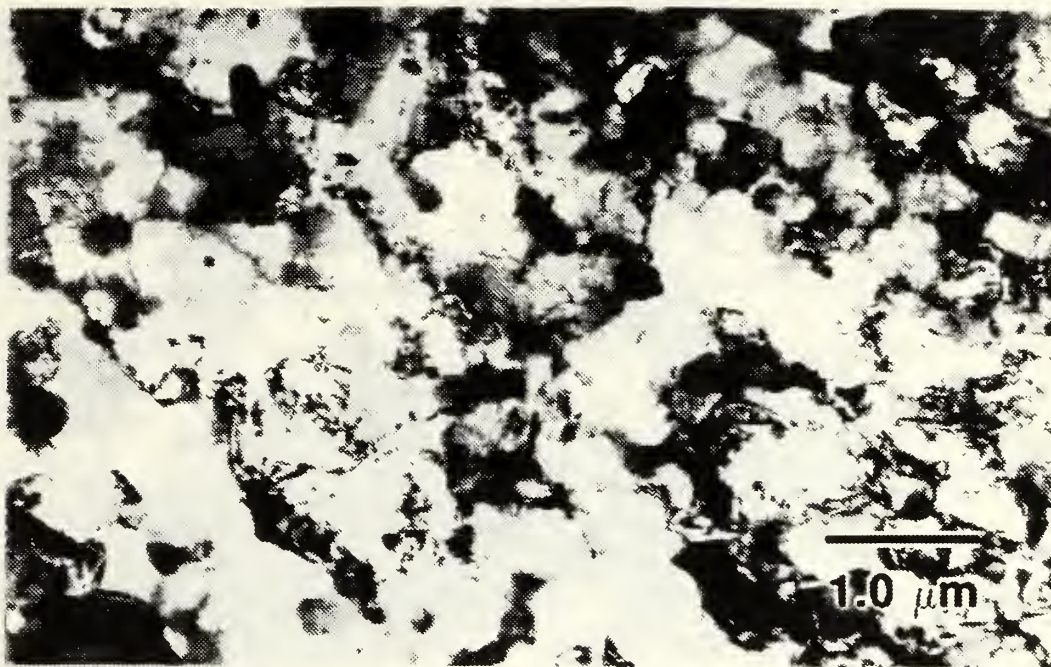
Figure 4.12. Bright field TEM micrograph of alloy 2090 from the grip section of a tensile sample tested at 300°C and $1.67 \times 10^{-1} \text{ s}^{-1}$ strain rate processed by TMP 2.

magnification as in Figures 4.13 and 4.14, TMP 6 seems to have a structure consisting of subgrains rather than grains, based on the contrast observed in TEM. This structure is more uniform and precipitates are well distributed. However, based on the limited contrast seen, continuous recrystallization has not occurred even with this increased reheating time. The intermetallic phases are not as coarse as seen in the Al-Mg alloys and since continuous recrystallization is similar to an advanced mechanism recovery, processing at a higher temperature may facilitate this recovery and enhance the likelihood of attaining a continuously recrystallized fine grain structure.

B. MECHANICAL PROPERTIES

Mechanical testing at elevated temperatures was conducted to investigate the deformation characteristics of processes TMP 1, TMP 2, TMP 6 and TMP 7. As previously described in Chapter III, tension testing was conducted at 300°C using strain rates varying from 6.67×10^{-5} to $1.67 \times 10^{-1} \text{ sec}^{-1}$ and then at 370°C, 440°C, 510°C using a single strain rate of $6.67 \times 10^{-4} \text{ sec}^{-1}$. The stress vs strain results of the tension tests are presented graphically in Figure 4.15 for TMP 2 and in Figure 4.16 in TMP 6. Plots for the other processes are included in Appendix B. The data for the ductility and flow stress as a function of strain rate as well as stress and ductility as a function of temperature will be presented throughout this chapter.

(a)



(b)



Figure 4.13. Bright field TEM micrograph, of alloy 2090 from the grip section of a tensile sample tested at 399°C and $1.67 \times 10^{-1} \text{ S}^{-1}$ strain rate processed by TMP 6.

(a)



(b)

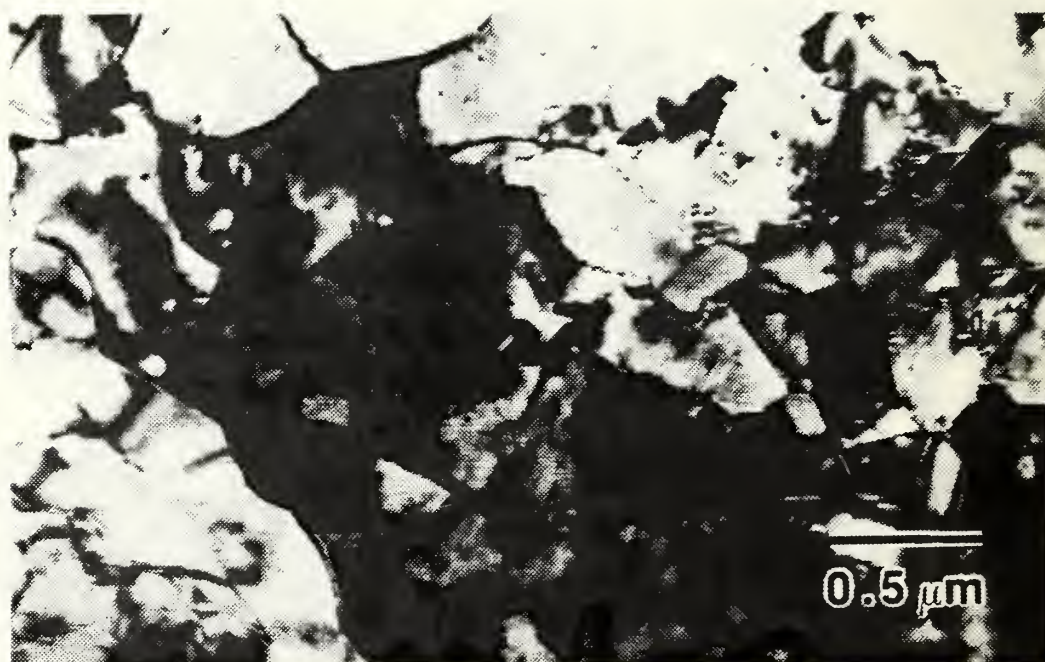


Figure 4.14. Bright field TEM micrographs, of alloy 2090 from the grip section of a tensile sample tested at 300°C and $6.67 \times 10^{-3} \text{ s}^{-1}$ strain rate processed by TMP 6.

1. Stress vs Strain Response

Typical Stress-Strain curves at 300°C for TMP 2 and TMP 6. Figures 4.15 and 4.16 show softening of the material more pronounced at high strain rates. TMP 6, with 30 minutes reheating time between passes, is clearly more ductile and weaker at low strain rates than TMP 2 with 4 minutes reheating time. Exactly the same results can be drawn when comparing TMP 1 (Figure B1) with TMP 7 (Figure B2). This means that the predominant variable in all TMPs is the reheating time between rolling passes. Comparison of such behavior at elevated temperature is normally done by evaluating the strain rate and temperature dependence of the strength and ductility.

2. Ductility, Stress vs Strain Rate Response

Ductility vs strain rate data are shown in Figure 4.17 while true stress vs strain rate data at 0.1 strain are shown in Figure 4.18 for the four TMPs at 300°C . Data for TMP 2 show a maximum elongation of only 75 percent and strain rate sensitivity coefficient about equal to 0.2. TMP 6 has considerably higher elongation, with a maximum value approaching 150 percent and a strain-rate sensitivity coefficient of about 0.28. Although a superplastic response was not obtained the beneficial effect of longer reheating time on ductility is evident. This mechanical response is consistent with the results obtained from microstructural observations. More ductility is expected for a more fully recovered and continuously recrystallized structure as observed with longer reheating time.

Comparison of these results with work by Munro [Ref. 32] shows the same trend as seen here of increased ductility with longer reheating

STRESS VS STRAIN (TMP2)

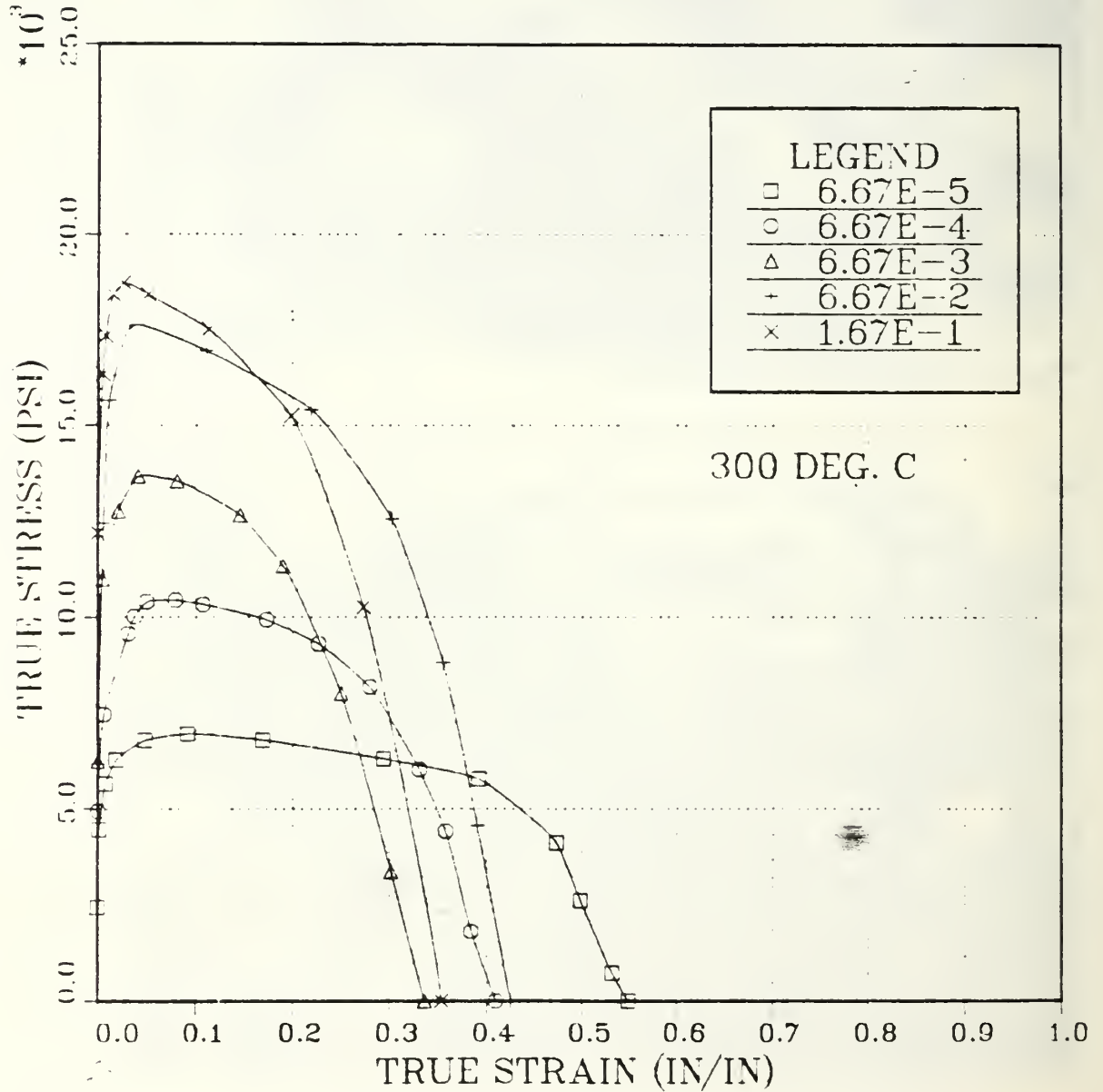


Figure 4.15. True stress versus true strain for tensile testing conducted at 300°C, for material processed by TMP 2, at various strain rates.

STRESS VS STRAIN (TMP6)

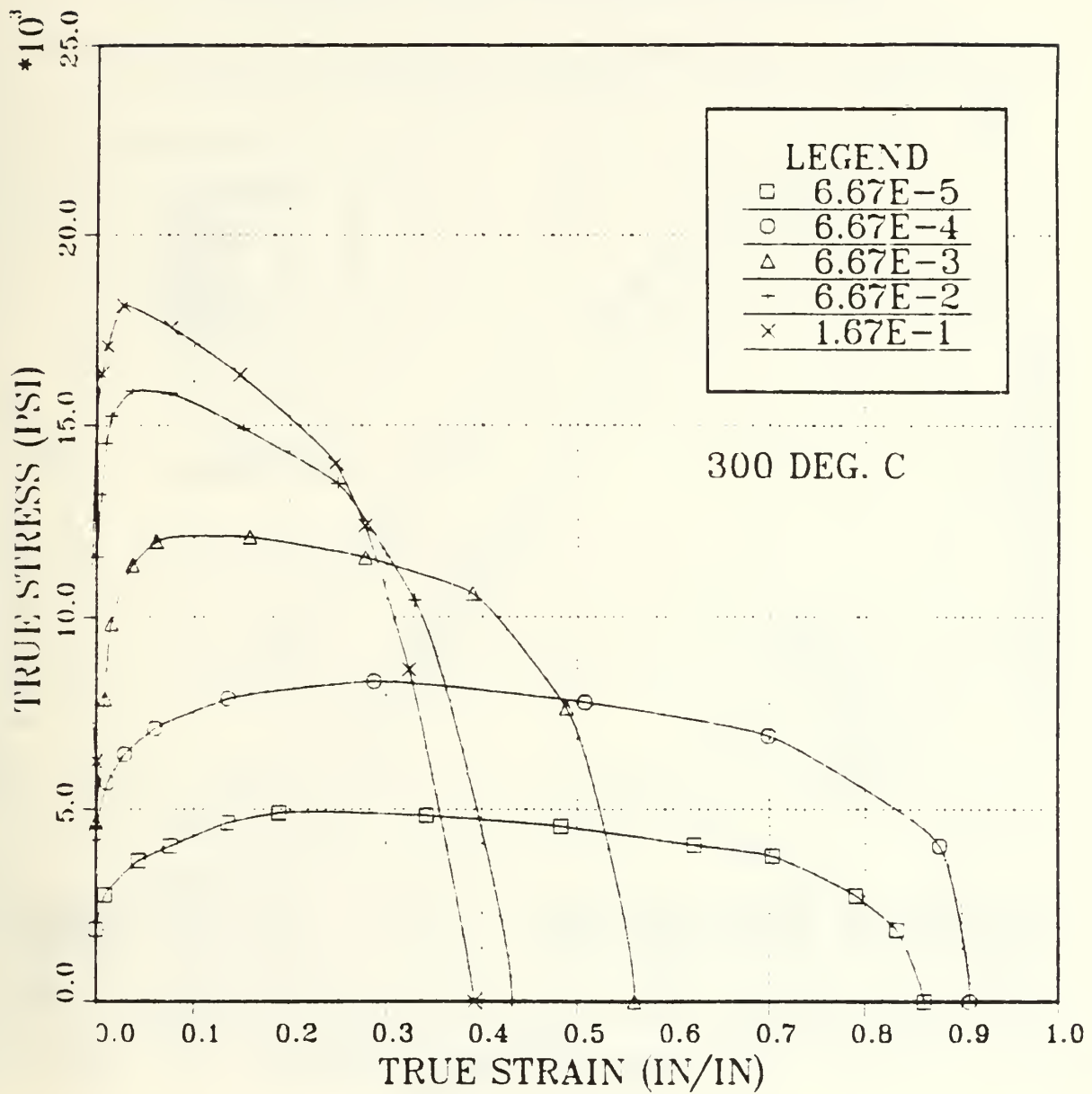


Figure 4.16. True stress versus true strain for tensile testing conducted at 300°C, for material processed by TMP 6, at various strain rates.

DUCTILITY VS STRAIN RATE

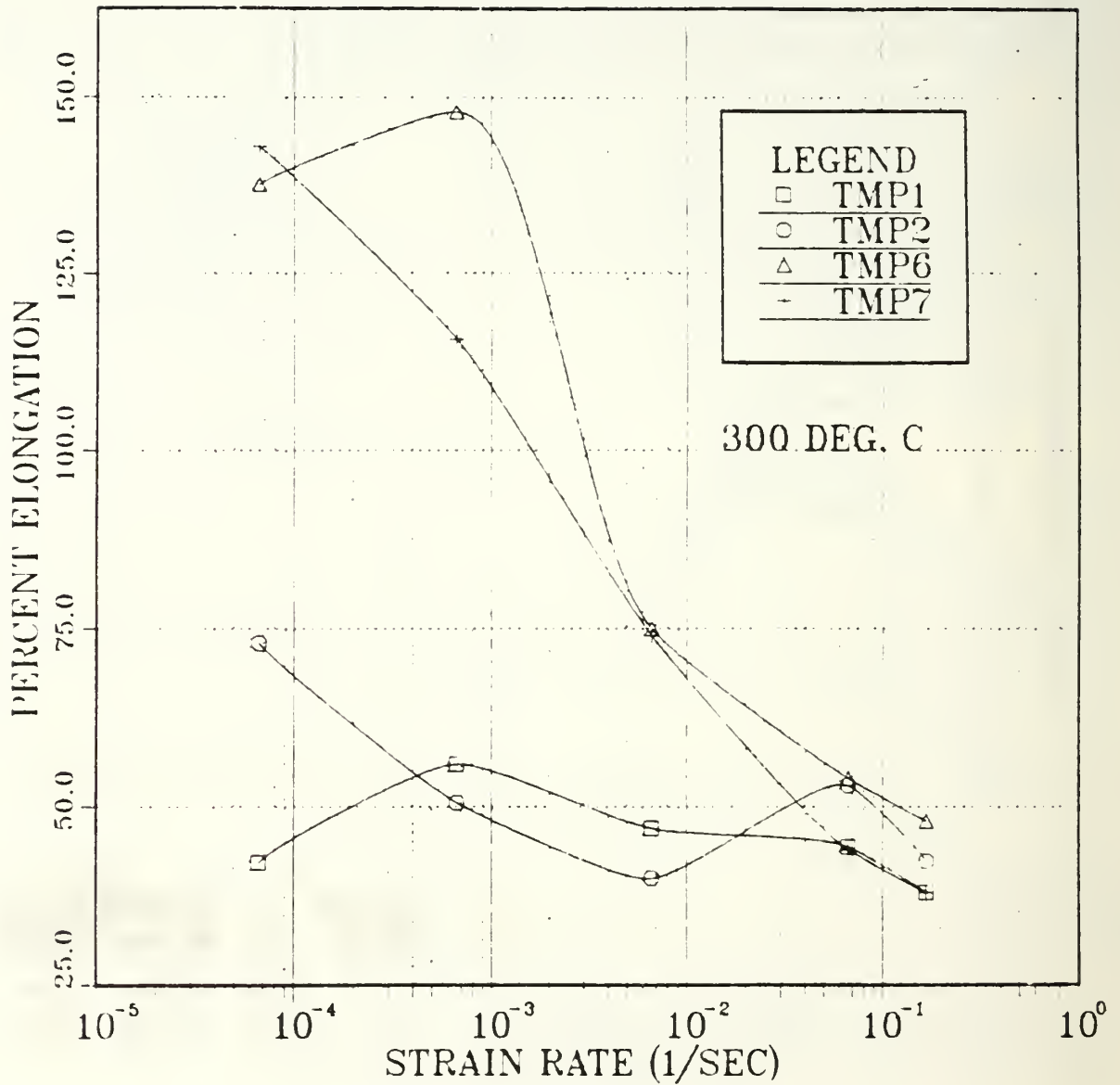


Figure 4.17. Ductility versus strain rate for tensile testing conducted at 300°C, for material processed by TMP 1, TMP 2, TMP 6, TMP 7.

STRESS VS STRAIN RATE

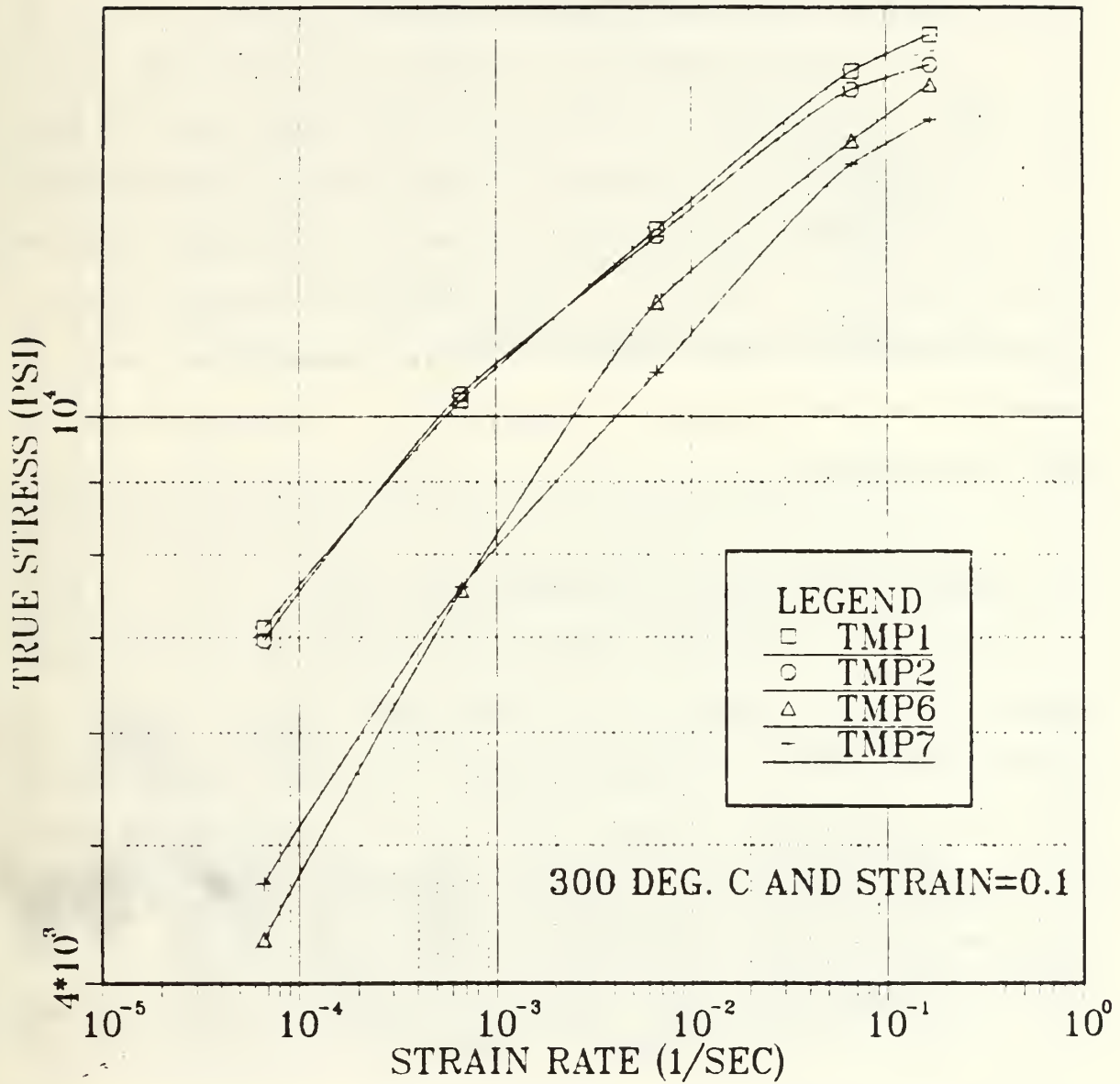


Figure 4.18. True stress at 0.1 strain versus strain rate for tensile testing conducted at 300°C for material processed by TMP 1, TMP 2, TMP 6, TMP 7.

between warm rolling passes. However, the peak ductility seen in the Al-Mg-Li alloy is greater than 1000 percent in conjunction with a larger value of $m \sim 0.45$. This suggests that some aspects of alloy composition promote recovery and continuous recrystallization.

3. Stress, Ductility vs Temperature Response

The effect of temperature on stress at $6.67 \times 10^{-4} \text{ sec}^{-1}$ strain rate and 0.1 strain and on ductility at the same strain rate are shown in Figure 4.19 and 4.20 respectively. Stress and ductility differences persist up to 500°C . These differences due to the reheating time are clear between TMP 2 and TMP 6. Longer reheating time again results in higher ductility and weaker material. Elevated temperatures result in weakening of the material as Figures 4.19, B.3, B.4 and B.5 show for both TMP 2 and TMP 6.

C. MICROSTRUCTURAL ANALYSIS OF DEFORMED CONDITIONS

TMP 2 and TMP 6 Gage Section micrographs at low and high magnification are shown in Figures 4.21, 4.22, 4.23 and 4.24 respectively. TMP 2 material has at most a recovered substructure. A continuously recrystallized grain structure has not been achieved in TMP 6 although the processing has resulted in better defined boundaries. Both TMPs retain dislocation substructure as shown on Figures 4.22 and 4.24. Both microstructures also are non uniform. There are regions where a well-recovered substructure exists, with fine precipitates $\sim 0.5 \mu\text{m}$ in size, similar to the structure of Aluminum-Magnesium-Lithium alloys where superplastic deformation is successful as documented by

STRESS VS TEMPERATURE

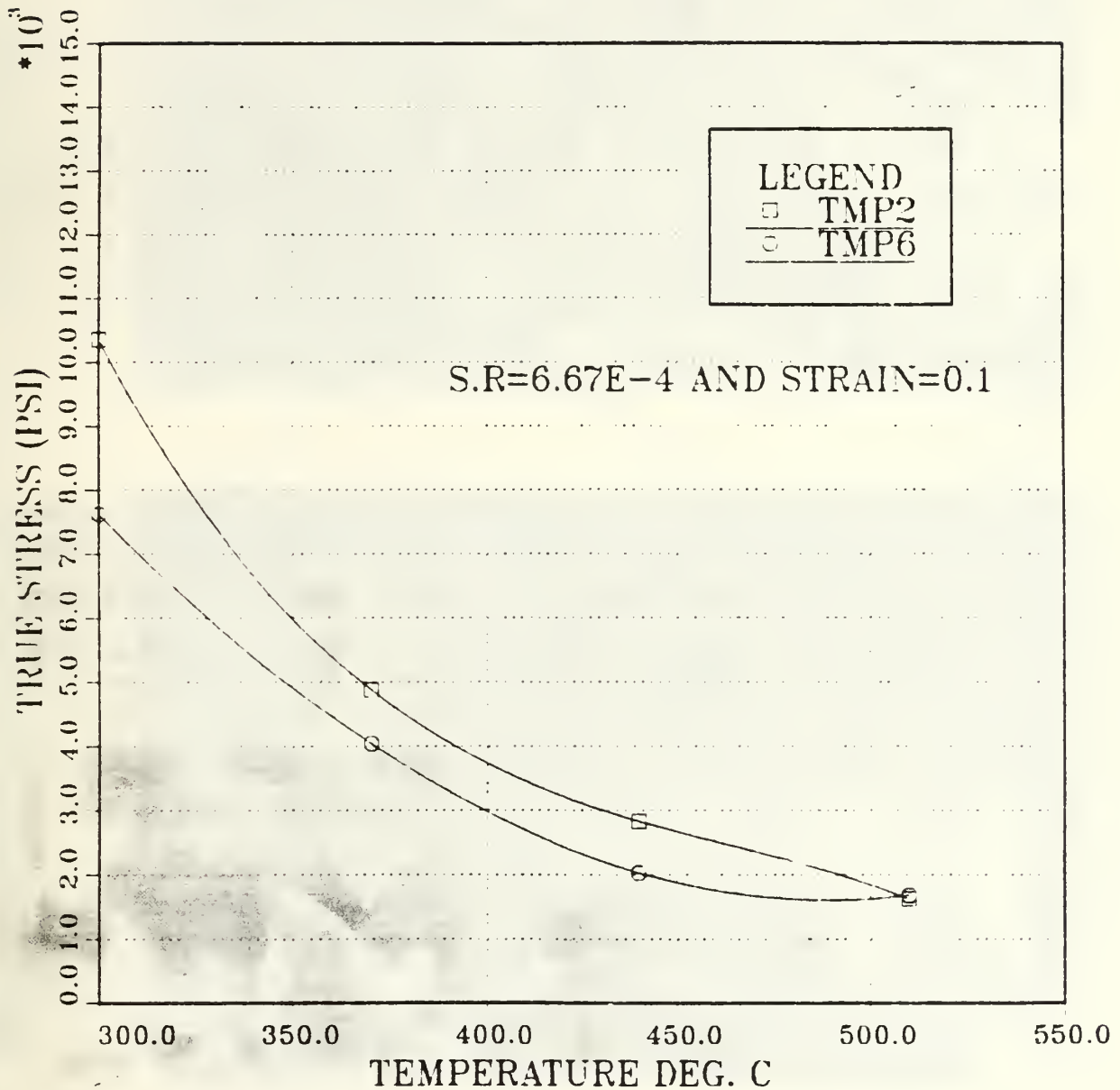


Figure 4.19. True stress at 0.1 strain and $6.67 \times 10^{-4} \text{ s}^{-1}$ strain rate versus temperature. Comparison between TMP 2 and TMP 6.

DUCTILITY VS TEMPERATURE

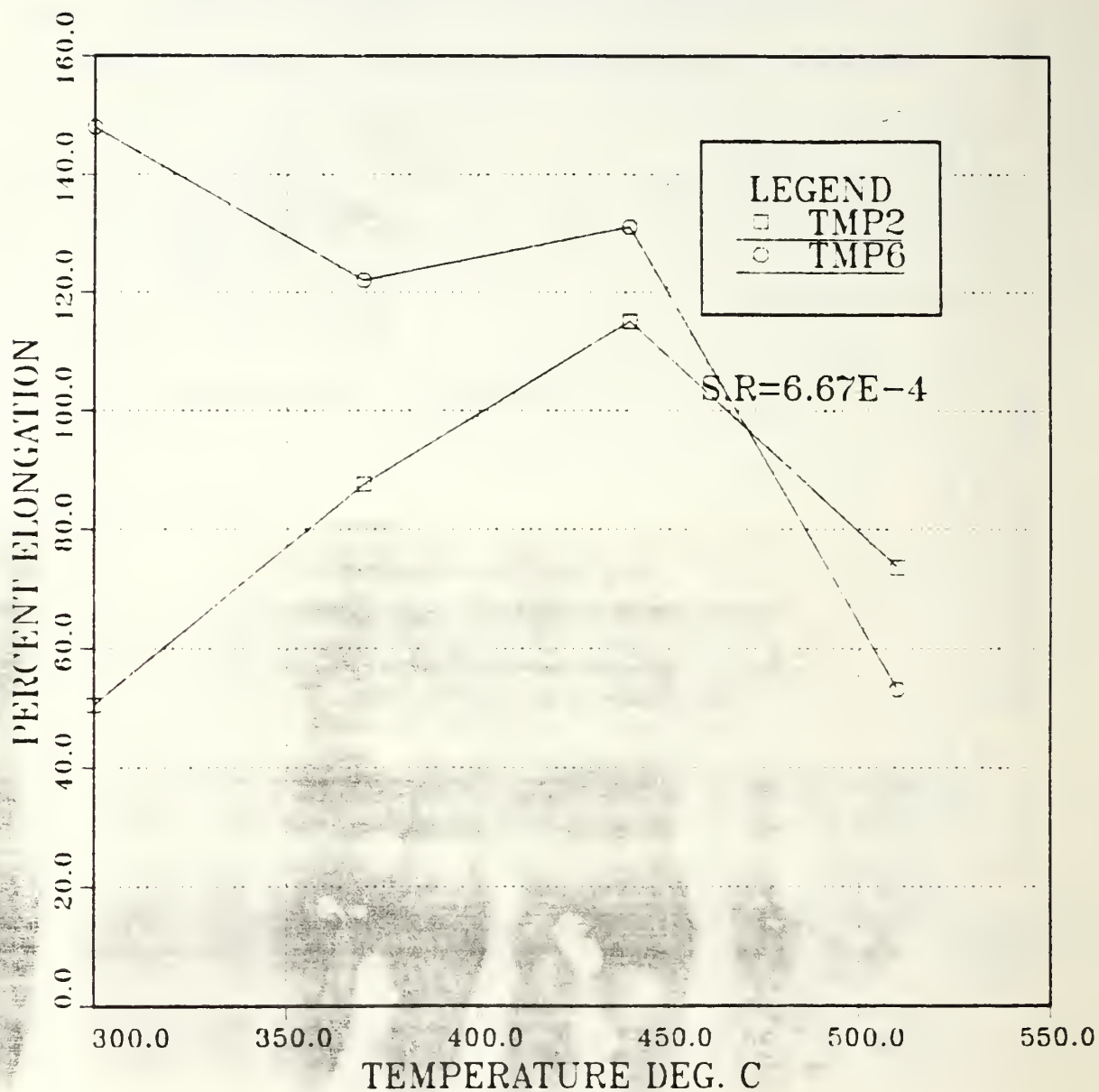
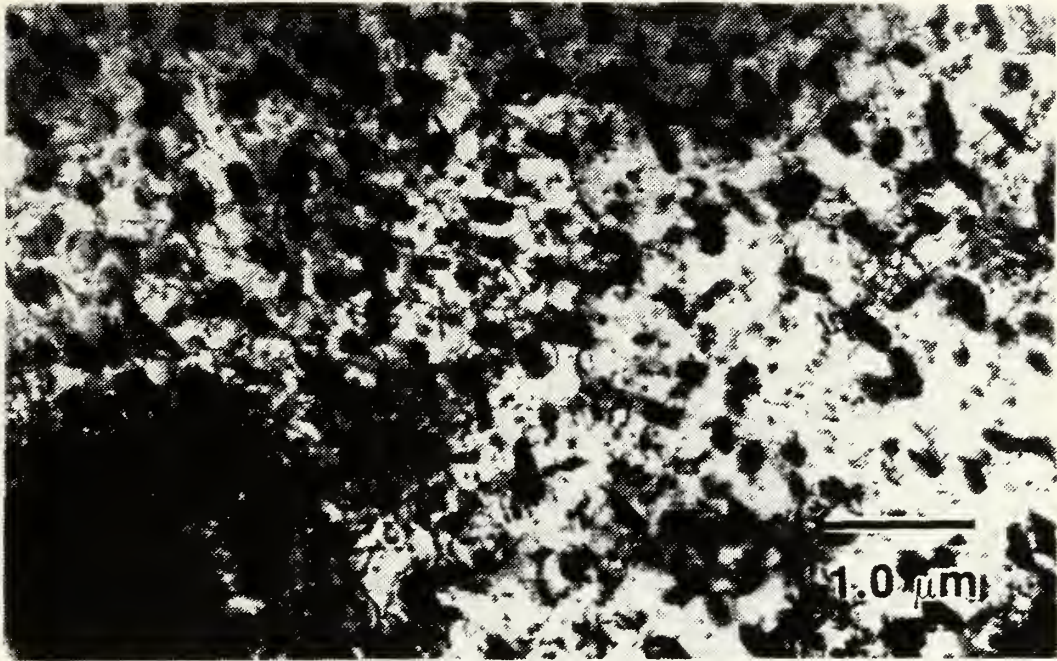


Figure 4.20. Ductility at $6.67 \times 10^{-4} \text{ s}^{-1}$ strain rate versus temperature. Comparison between Tmp 2 and Tmp 6.

(a)



(b)



Figure 4.21. Bright field TEM micrographs of alloy 2090 from the gage section of a tensile sample tested at 300°C and $6.67 \times 10^{-4} \text{ s}^{-1}$ strain rate.

(a)



(b)

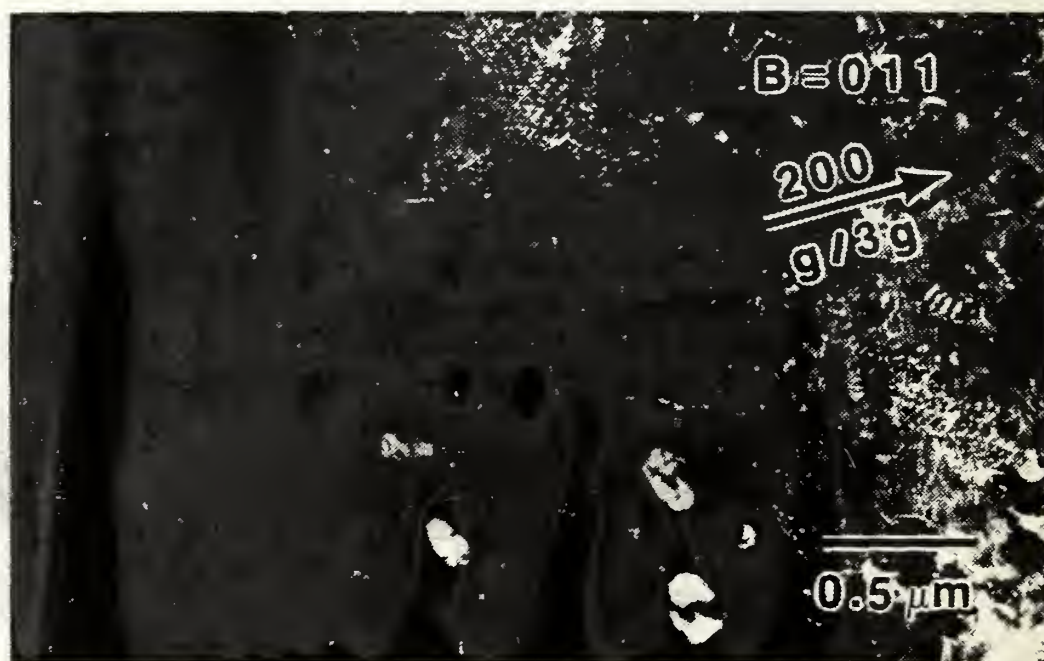


Figure 4.22. TEM micrographs, (a) bright field, (b) dark field, of alloy 2090 from the gage section of a tensile sample tested at 300°C and $6.67 \times 10^{-4} \text{ s}^{-1}$ strain rate processed by TMP 2.

(a)

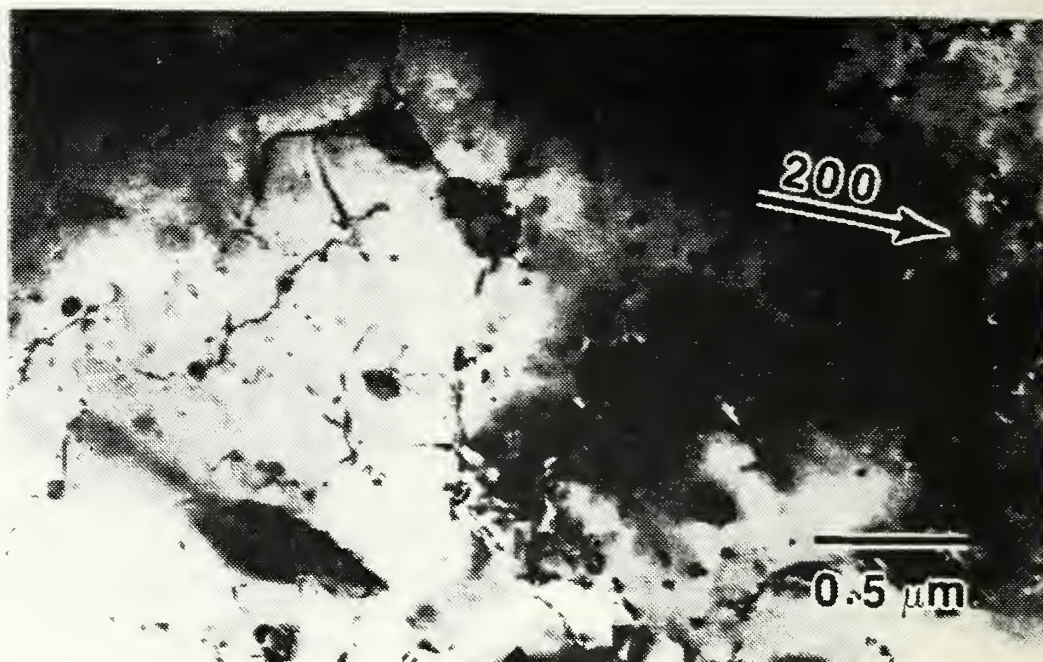


(b)



Figure 4.23. Bright field TEM micrographs, of alloy 2090 from the gage section of a tensile sample tested at 300°C and $6.67 \times 10^{-4} \text{ s}^{-1}$ strain rate processed by TMP 6.

(a)



(b)

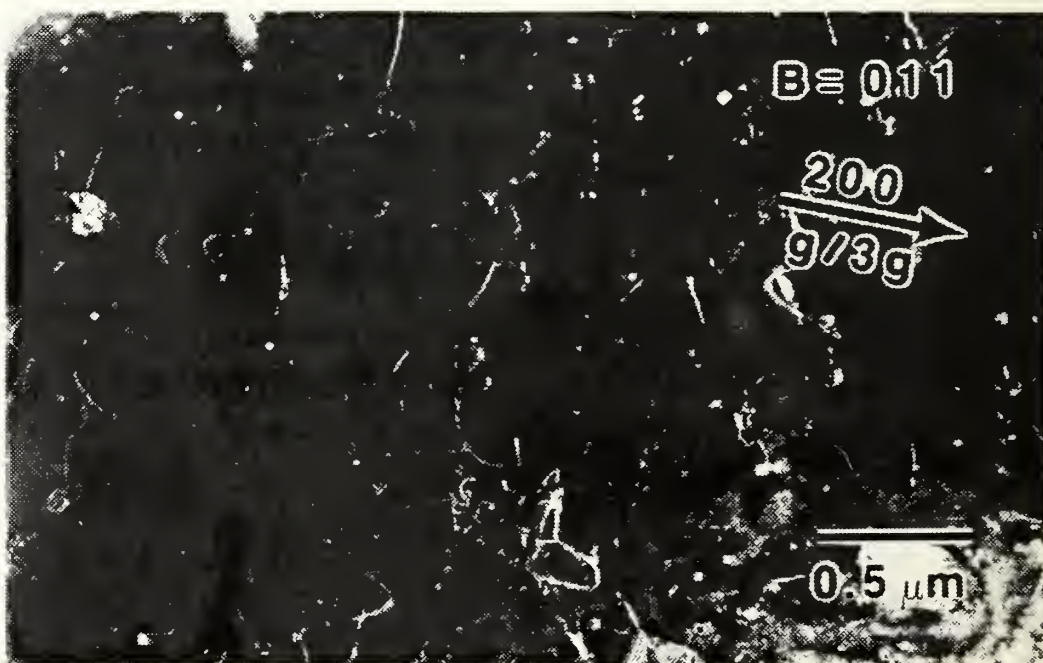


Figure 4.24. TEM micrographs, (a) bright field, (b) dark field, of alloy 2090, from the gage section of a tensile testing at 300°C and $6.67 \times 10^{-4} \text{ s}^{-1}$ strain rate processed by TMP 6.

Munro [Ref. 32]. There are other regions of large grain size and coarser precipitates, much greater than 0.5 μm in size.

These observations suggest that a continuously recrystallized structure is attainable in the 2090 alloy, although non uniform distribution of alloying additions may present a problem. Continuous recrystallization is a recovery process and thus the reaction rate is diffusion controlled. Thus,

$$\frac{1}{t_{\text{recovery}}} \text{ rate} = B \exp(-Q/RT)$$

where t_{recovery} is the time allowed during reheating, B is a constant, Q is the activation energy for the recovery, process R is the gas constant, and T is the temperature. From this, it can be seen that the effect of increased reheating (recovery) time can also be produced by increased temperature. This would also facilitate coarsening of second phase particles to enhance their interaction with the recovering substructure.

D. PHASES OBSERVED

The precipitation sequences in Aluminum-Copper-Lithium alloys are not well-defined, particularly for the various metastable phases, as they are mentioned in Chapter II, which may precede the equilibrium binary and ternary precipitates in this system.

The phase we might expect to appear in 2090 according to Mondolfo, Yoshida and coworkers, Lee and coworkers, Colvin and coworkers Ref. [4,29,30,31], respectively, are T_1 , T_2 , θ' , δ , δ' , I and β' with more

information about them presented in Table 7. During TEM examination plate-like, directional, intragranular second phase precipitates appeared in the microstructure and according to the above mentioned references there is a strong evidence that this is T_1 ($LiCuAl_2$) phase. Another precipitate exhibiting five-fold diffraction symmetry and irregular shape was detected with TEM. According to Cassada and coworkers this is the I-phase of unknown composition with a complex crystal structure.

Table 7
Possible Phases in 2090

<u>Phase</u>	<u>Composition</u>	<u>Location*</u>	<u>Shape</u>	<u>Habit Plane</u>
T_1	$LiCuAl_2$	GB, GI	Platelike	111
T_2	$Li_3CuAl_{6(5)}$	GB, GI	Platelike Irregular	100
θ'	$CuAl_2$	GI	Platelike	100
δ'	$LiAl$	GB, GI	Platelike	100
δ	$LiAl_3$	GI	Spherical	111
I	?	GB	Irregular	100
β	$ZrAl_3$	GI	Spherical	

*GB = Grain Boundaries

GI = Grain Interior

V. CONCLUSIONS

A. CONCLUSIONS

The following conclusions are drawn from this research:

1. Optical microscopy revealed the following:

- a. The fine precipitate produced, likely to be $T_1(Al_2CuLi)$, is more uniformly distributed in the material with the longer reheating time (30 mins) during warm rolling. With short reheating time (4 mins) it is seen predominantly at grain boundaries.
- b. Aging time does not significantly change the second phase precipitate size and distribution.

2. Transmission Electron Microscopy revealed the following:

- a. The presence of the I- and $T_1(Al_2CuLi)$ phases in the material with short reheating time during warm rolling only.
- b. A fine and uniformly distributed $T_2(Al_5Li_3Cu)$ phase was present at both short and long reheating times with a larger volume fraction present for the short reheating time.
- c. Tension tested material rolled with short reheating time, exhibits a structure approximating to the as-rolled microstructure, with some dislocation rearrangement in evidence. A recovered substructure with noticeable misorientation between subgrains was observed in the

material rolled with long reheating time during warm rolling.

3. Aging prior to warm rolling does not significantly affect the ductility or the strength of the material in subsequent elevated temperature testing.
4. Increased reheating time between rolling passes, from 4 to 30 minutes during warm rolling, resulted in:
 - a. Enhancement of the warm temperature ductility
 - b. A decrease in flow stress
 - c. An increase in the strain-rate sensitivity coefficient
 - d. A softer and weaker material at a given strain rate as a function of temperature from 300°C to 450°C, while at the highest test temperature used the two conditions were identical in behavior.
5. Effects of the increased reheating time persist at least to 450°C, resulting in higher ductility for a given strain-rate.

VI. RECOMMENDATIONS

The following are recommendations for further study:

1. Conduct the same series of experiments done in this research but utilizing higher warm rolling and tension test temperatures, 350°C and 400°C. The results should be compared with the work of H. Yoshida and coworkers [Ref.29] in which superplasticity was obtained in the above temperature range.
2. Warm roll the material using the light reduction schedule, to study the effect it has on the ductility and strength of this alloy.
3. Conduct the same series of experiments done in this research using uniformly cold worked material with thickness reductions of 0%, 1%, 2%, 3%, 5%, and 15%, to study the effect of cold working on the T_1 phase morphology and distribution.

APPENDIX A
COMPUTER PROGRAM

```
CHARACTER*10  FN,ON,AGAIN
INTEGER N
REAL X,LOAD,ELONG,MF,CF,AREA,SENG,ENG,STRUE,ETRUE
PRINT*, 'INPUT THE FILE TO BE PROCESSED:'
READ '(A)',FN
PRINT *,FN
ON = 'OUT'//FN
PRINT *, ON
CALL EXCMS('FILEDEF 7 DISK ' // FN // 'DATA' )
CALL EXCMS('FILEDEF 8 DISK ' // ON // 'DATA' )
READ (7,*) N,CF,MF,AREA
DO 100 I = 1,N
  READ (7,*) X,LOAD
  ELONG = (X/MF)*CF
  SENG = LOAD / AREA
  ENG = ELONG / .5
  STRUE = SENG * (1 + ENG)
  ETRUE = LOG(1 + ENG)
  FORMAT (1X,F8,2,2X,F7.4,2X,F8.2,2X,F7.4)
  WRITE (8,50) STRUE,ETRUE,SENG,ENG
STOP
END
```

APPENDIX B
TENSILE TEST DATA

STRESS VS STRAIN (TMP1)

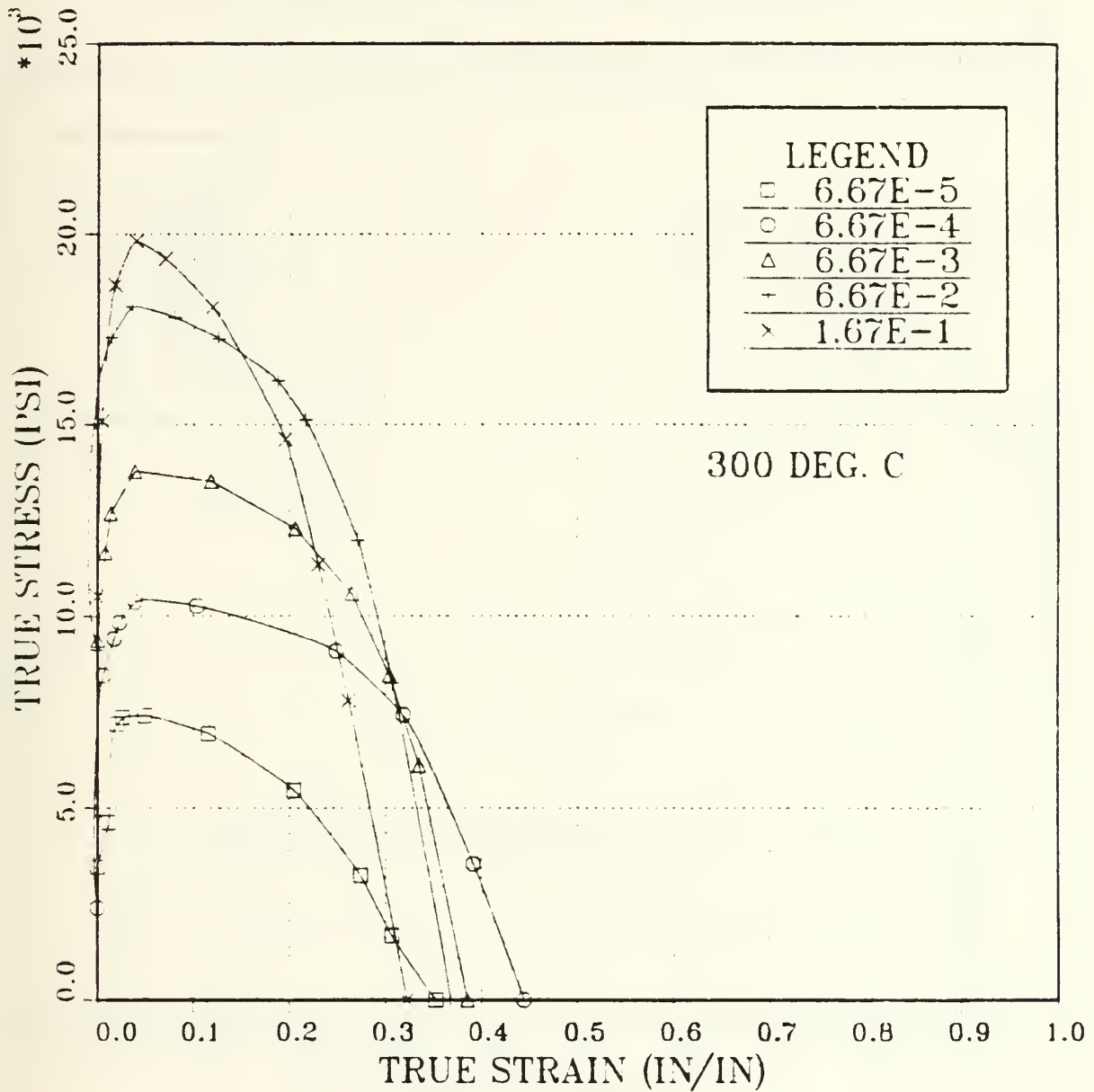


Figure B.1. True stress versus true strain for tensile testing conducted at 300°C, for material processed by TMP1 at various strain rates.

STRESS VS STRAIN (TMP7)

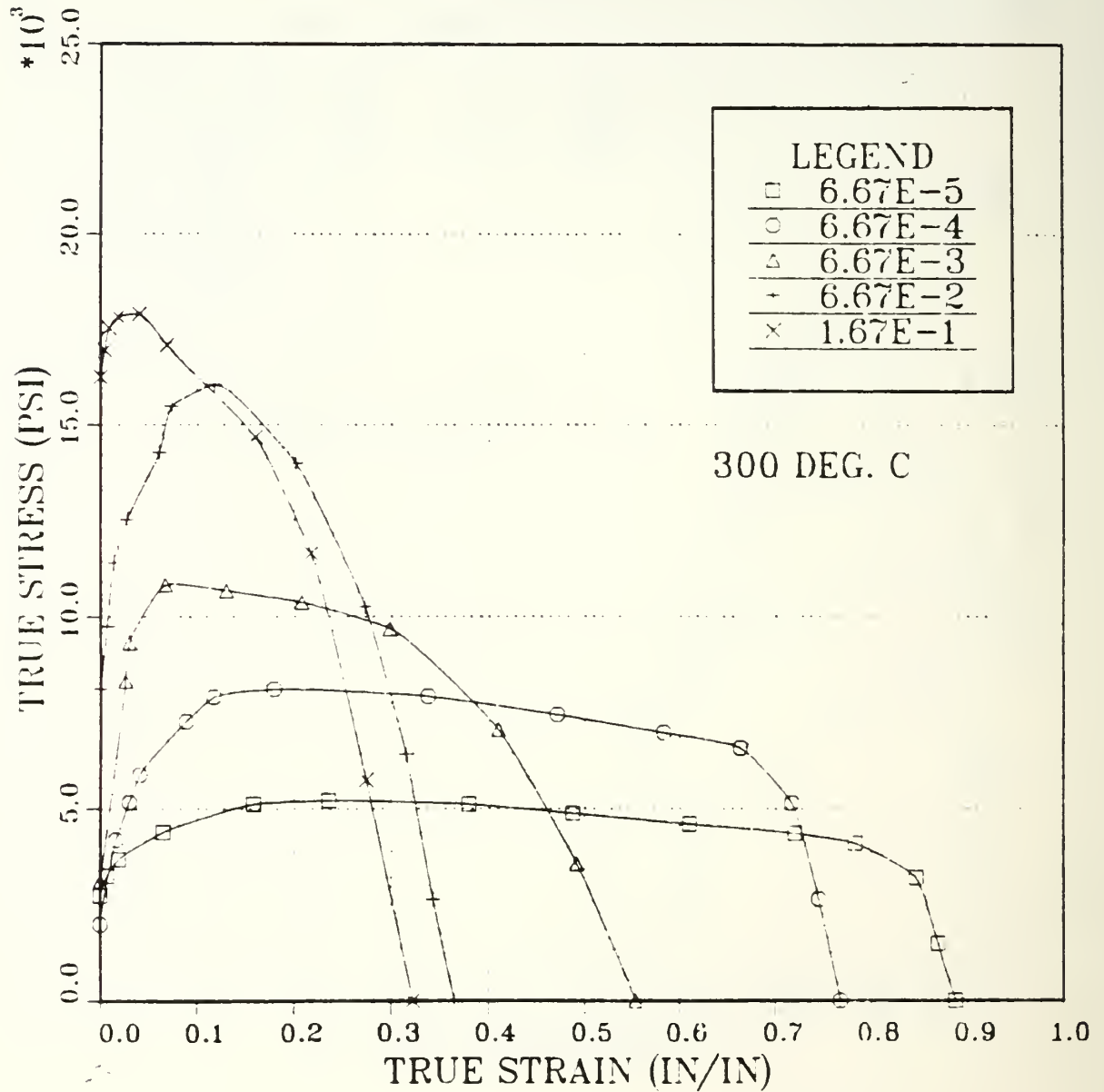


Figure B.2. True stress versus true strain for tensile testing, conducted at 300°C, for material processed by TMP 7.

STRESS VS STRAIN (6.67E-4)

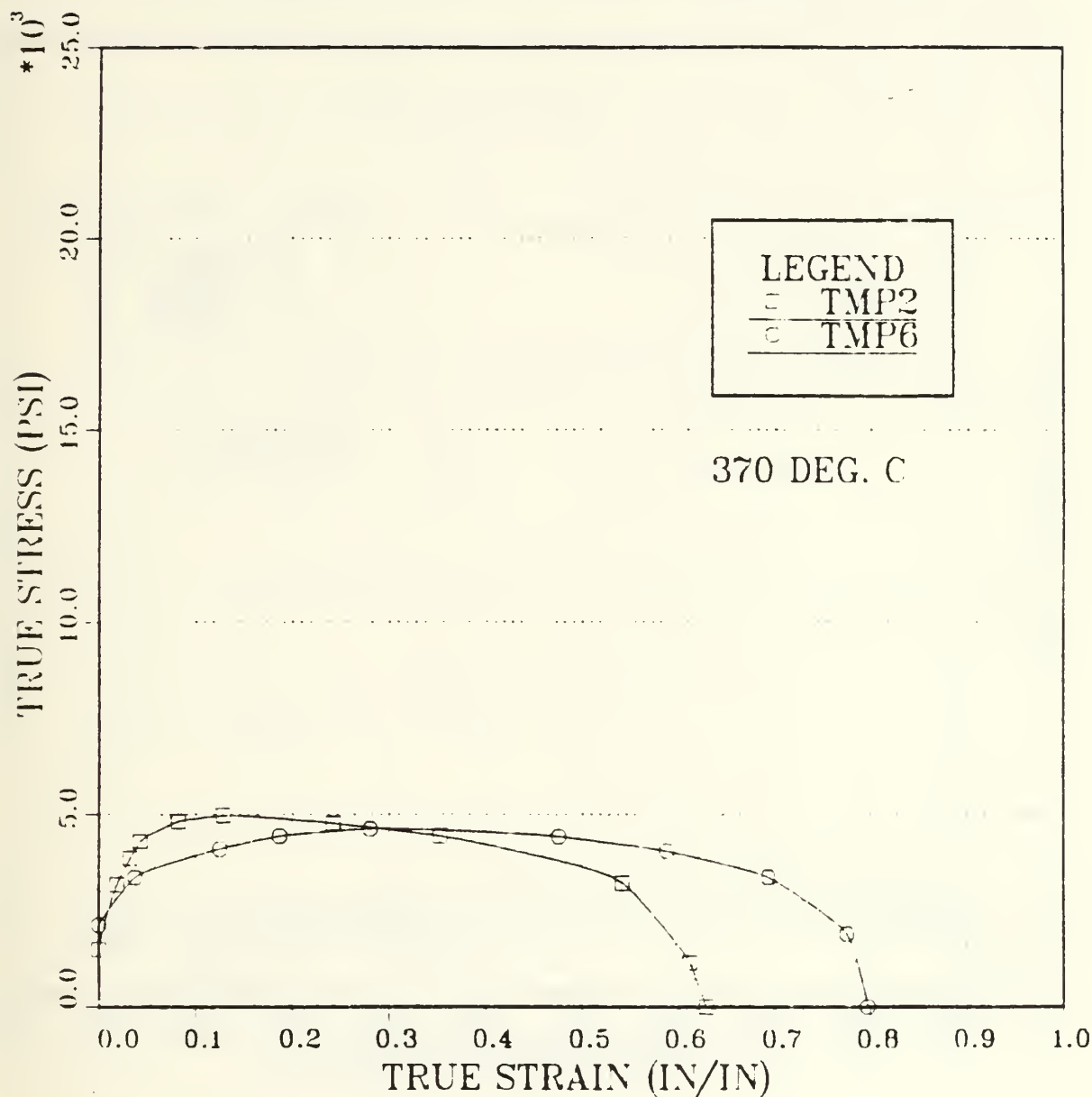


Figure B.3. True stress at $6.67 \times 10^{-4} \text{ s}^{-1}$ strain rate versus true strain for tensile testing conducted at 370°C, for material processed by TMP 2 and TMP 6.

STRESS VS STRAIN (6.67E-4)

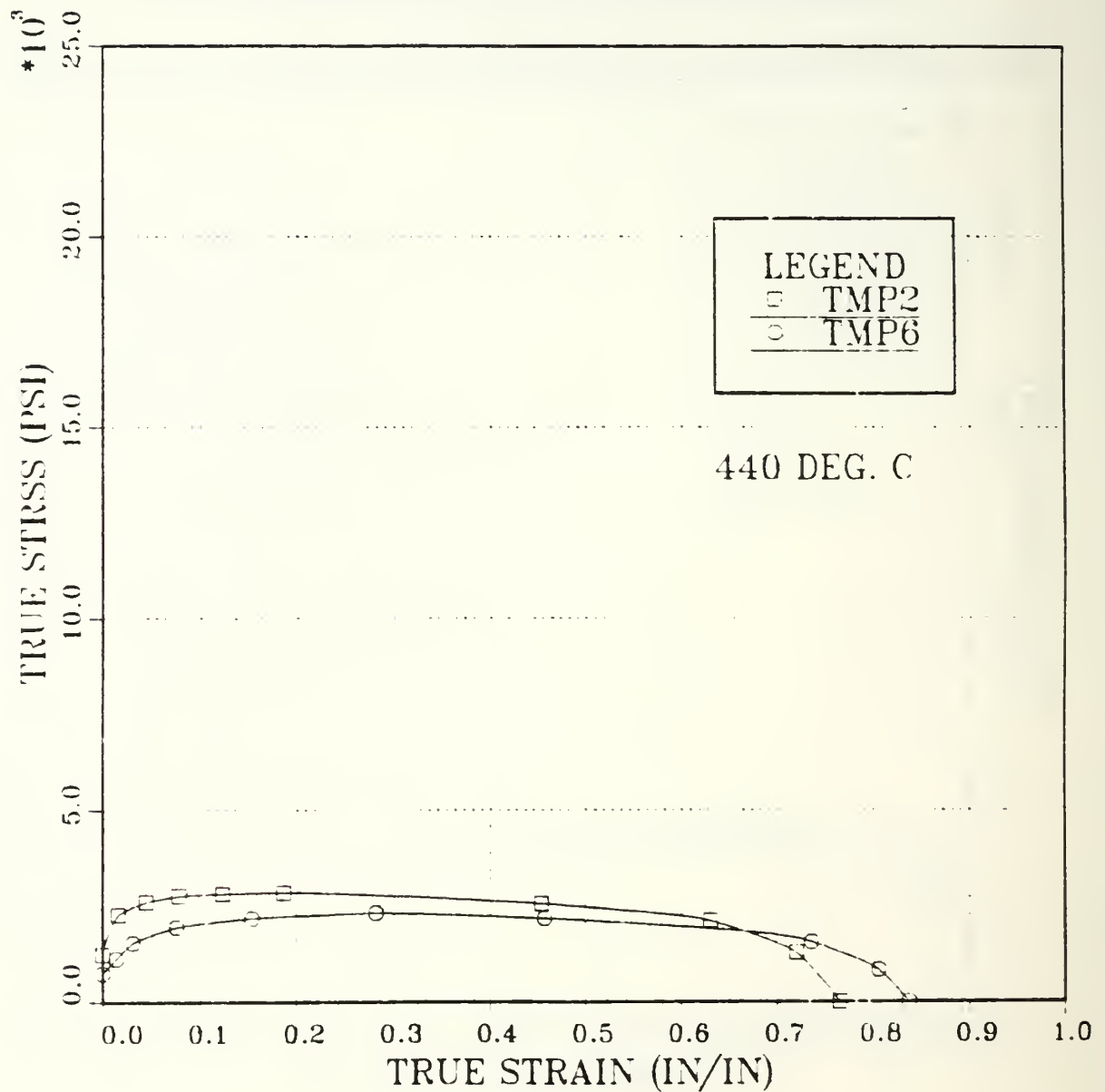


Figure B.4. True stress at $6.67 \times 10^{-4} \text{ s}^{-1}$ strain rate versus true strain for tensile testing conducted at 440°C , for material processed by TMP 2 and TMP 6.

STRESS VS STRAIN (6.67E-4)

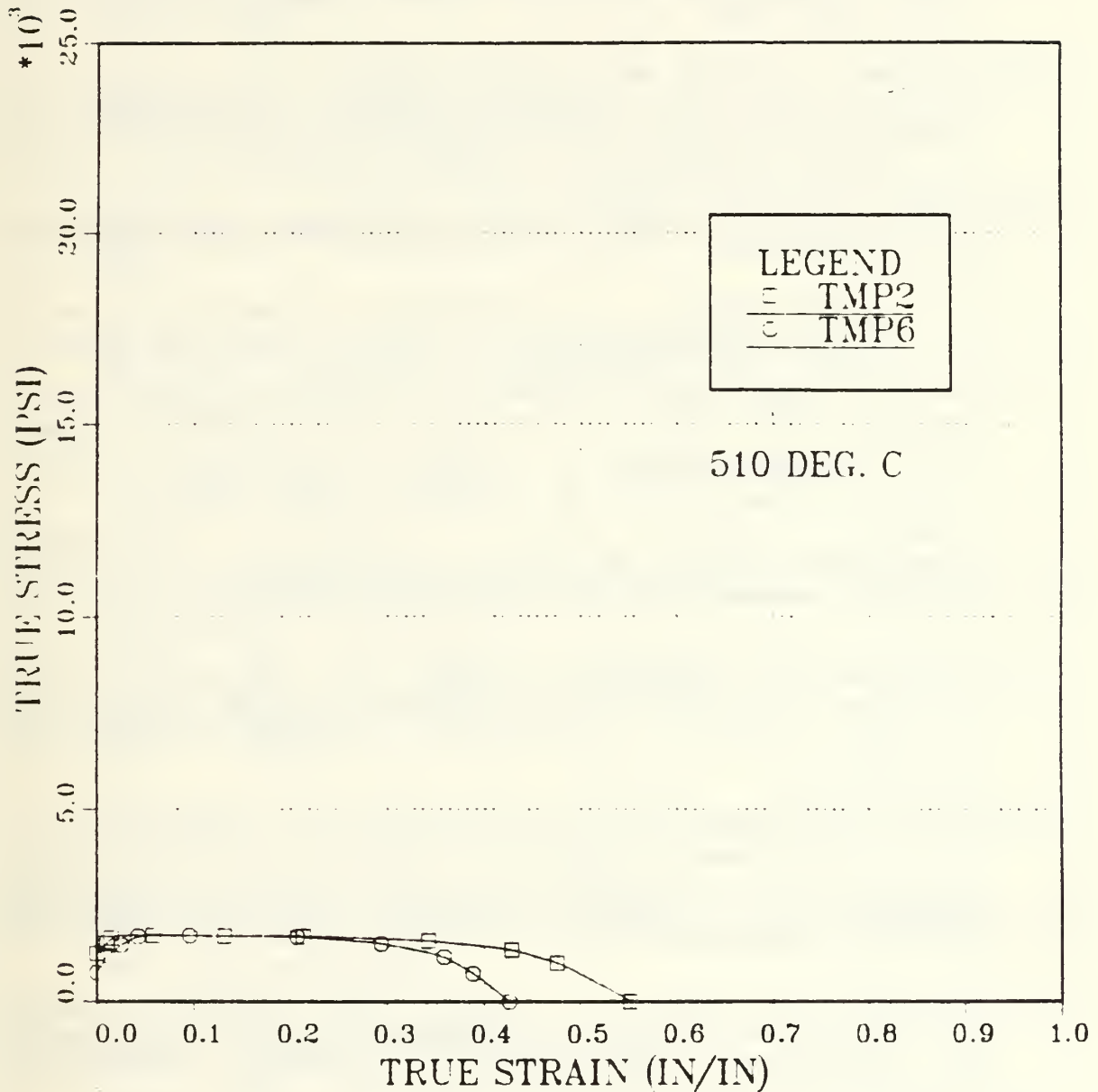


Figure B.5. True stress at $6.67 \times 10^{-4} \text{ s}^{-1}$ strain rate versus true strain for tensile testing conducted at 510°C , for material processed by TMP 2 and TMP 6.

LIST OF REFERENCES

1. Massalski, T. B., Binary Alloy Phase Diagrams, vol. 1, American Society for Metals, 1986.
2. Starke, E. A., Sanders, T. H. and Palmer, I. G., "New Approaches to Alloy Development in the Al-Li System", Journal of Metals, pp. 24-32, August 1981.
3. Sankaran, K. K. and Grant, N. J., "Structure and Properties of Splat Quenched 2024 - Aluminum Containing Lithium Additions", Aluminum-Lithium Alloys, by T. H. Sanders and E. A. Starke, vol. 1, pp. 205-227, The Metallurgical Society of AIME, 1980.
4. Mondolfo, L. F., Aluminum Alloys: Structure and Properties, Butterworth, 1976.
5. Sigli, C. and Sanchez, J. M., "Calculation of Phase Equilibrium in Al-Li Alloys", Acta Metallurgica, vol. 34, pp. 1021-1028, 1986.
6. Gu, B. P., Mahalingam, K., Liedl, G. L. and Sanders, T. H., "The S' (Al Li) Particle Size Distributions in a Variety of Al-Li Alloys", Aluminum-Lithium Alloys, by C. Baker, P. J. Gregson, S. J. Harris and C. J. Peel, vol. III, The Institute of Metals, 1986.
7. Wadsworth, J., Pelton, A. R. and Lewis, R. E., "Superplastic Al-Cu-Li-Mg-Zr Alloys", Metallurgical Transactions A, vol. 16A, pp. 2319-2332, December 1985.
8. Lloyd, D. J. and Moore, D. M., "Aluminum Alloy Design for Superplasticity", Superplastic Forming of Structural Alloys, Conference Proceedings of TMS-AIME and ASM 1982, N. E. Parton and C. H. Hamilton, eds., pp. 147-169, The Metallurgical Society of AIME, 1982.
9. Cassada, W. A., Shiflet, G. J. and Starke, E. A., "Characterization of two Grain Boundary Precipitates in Al-Li-Cu Alloys with Electron Micro-Diffraction", Aluminum Alloys their Physical and Mechanical Properties, vol. II, Conference Proceedings, Engineering Materials Advisory Services, LTD., 1986.
10. Rioja, R. J. and Bretz, P. E., "Precipitation Reactions, Strength and Toughness of Al-Li-Cu Alloys", Aluminum Alloys their Physical and Mechanical Properties, vol. III, Conference Proceedings, Engineering Materials Advisory Services, LTD., 1986.
11. Hardy, H. K. and Silcock, J. M., "The Phase Sections at 500 C and 350 C of Al-rich Al-Cu-Li Alloys", Journal of the Institute of Metals, vol. 84, pp. 423-428, 1955-56.

12. Silcock, J. M., "The Structural Aging Characteristics of Aluminum-Copper-Lithium Alloys", Journal of the Institute of Metals, vol. 88, pp. 357-364, 1959-60.
13. Huang, J. C. and Ardell, A. J., "Microstructural Evolution in two Al-Li-Cu Alloys, Aluminum-Lithium Alloys, by C. Baker, P. J. Gregson, S. J. Harris and C. J. Peel, vol. III, The Institute of Metals, 1986.
14. Sanders, T. H., "Al-Li-X Alloys - An Overview", Aluminum-Lithium Alloys, by T. H. Sanders and E. A. Starke, vol. I, pp. 63-67, The Metallurgical Society of AIME, 1980.
15. Cieslak, S. J. and Hart, R. M., ALCOA Alithalite Alloy 2090 Technical Information, Paper presented at the 17th International Sampe Technical Conference 1985 October 22-24, Kiamesha Lake, NY, 1985.
16. Bretz, P. E. and Sawtell, R. R., "Alithalite Alloys: Progress Products and Properties", Al-Li Alloys, Paper Presented at the 3rd International Aluminum-Lithium Conference, University of Oxford, July 1985.
17. Underwood, E. E., "A Review of Superplasticity and Related Phenomena", Journal of Metals, pp. 914-919, December 1962.
18. Sherby, O. D. and Wadsworth, J., "Development and Characterization of Fine-Grain Superplastic Materials", Deformation, Processing, and Structure, pp. 354-384, 1987.
19. McNelley, T. R. and Hales, S. J., "Superplastic Aluminum Alloys", Naval Research Reviews, vol. 39.1, pp. 51-57, Office of Naval Research, 1987.
20. Wert, J. A. and Paton, N. E., "Enhanced Superplasticity and Strength in Modified Ti-6Al-4v Alloys", Metalurgical Transactions A, vol. 14A, pp. 2535-2544, December 1983.
21. Hales, S. J. and McNelley, T. R., "Microstructural Evolution by Continuous Recrystallization in a Superplastic Al-Mg Alloy", in press, Acta Metalurgica.
22. Annual Book of ASTM Standards, vol. 02.02, pp. 1044-1055, American Society for Testing and Materials, 1986.
23. Source Book on Selection and Fabrication of Aluminum Alloys, American Society for Metals, 1978.
24. Anamet Laboratories, Inc., Hayward, California, Laboratory Report No. 887.180, 25 August 1987.

25. McNelley, T. R., Lee, E. W. and Garg, A., "Superplasticity in Thermomechanically Processed High-Mg, Al-Mg-X Alloys", Aluminum Alloys their Physical and Mechanical Properties, vol. II, Conference Proceedings, Engineering Materials Advisory Services, LTD., 1986.
26. Scott, T. E., "Ingot and Billet Processing of Aluminum Alloys", Aluminum Alloys their Physical and Mechanical Properties, vol. III, Engineering Materials Advisory Services, LTD., 1986.
27. Wise, J. E., The Influence of Total Strain, Strain Rate and Reheating Time During Warm Rolling and the Superplastic Ductility of an Al-Mg-Zr Alloy, M. S. Thesis, Naval Postgraduate School, Monterey, California, March 1987.
28. Metals Handbook, 9th ed., vol. 9, pp. 351-360, American Society for Metals, 1986.
29. Yoshida, H. and coworkers, "The Effect of Grain Boundary Precipitation on the Superplasticity of Al-Li Alloys", 4th International Al-Li Conference in Paris, France, 10-12 June 1987.
30. Lee, E. W. and Frazier, W. E., "The Effect of Stretch on the Microstructure and Mechanical Properties of 2090 Al-Li", in press, Scripta Metalurgica.
31. Colvin, E. L., Murtha, S. J. and Wyss, R. K., "Stress Corrosion Cracking Susceptibility of Alloy 2090", Aluminum Alloys their Physical and Mechanical Properties, vol. III, Engineering Materials Advisory Services, LTD, 1986.
32. Munro, I., "Optimizing Superplastic Response in Lithium Containing Aluminum-Magnesium Alloys", M. S. Thesis, Naval Postgraduate School, Monterey, California, December 1987.

INITIAL DISTRIBUTION LIST

	No. Copies
1. Defense Technical Information Center Cameron Station Alexandria, Virginia 22304-6145	2
2. Library, Code 0142 Naval Postgraduate School Monterey, California 93943-5000	2
3. Department Chairman, Code 69Hy Department of Mechanical Engineering Naval Postgraduate School Monterey, California 93943-5000	1
4. Professor T. R. McNelley, Code 69Mc Department of Mechanical Engineering Naval Postgraduate School Monterey, California 93943-5000	5
5. Dr. S. J. Hales, Code 69He Department of Mechanical Engineering Naval Postgraduate School Monterey, California 93943-5000	1
6. Naval Air Systems Command, Code AIR 931 Naval Air Systems Command Headquarters Washington, DC 20361	1
7. Hellenic Air Force General Staff 2nd Branch, Education Department Stratopedon Papagou GR. 155.61 Holargos Athens GREECE	5
8. CPT Procopis T. Spiropoulos Lykourgou St 172 Kallithea, Athens GREECE	5
9. Dr. Eui-Whee Lee, Code 6063 Naval Air Development Center Warminster, Pennsylvania 18974	1

Thesis

S66857 Spiropoulos

c.1 Thermomechanical processing of Al alloy 2090 for grain refinement and superplasticity.

Thesis

S66857 Spiropoulos

c.1 Thermomechanical processing of Al alloy 2090 for grain refinement and superplasticity.



thesS66857

Thermomechanical processing of Al alloy



3 2768 000 78654 5

DUDLEY KNOX LIBRARY C1